
Article:
Xie, P., Ding, H., Ingham, D.B. et al. (2 more authors) (2020) Analysis and prediction of the gas-liquid interfacial area for droplets impact on solid surfaces. Applied Thermal Engineering, 178. 115583. ISSN 1359-4311

https://doi.org/10.1016/j.applthermaleng.2020.115583

Analysis and prediction of the gas-liquid interfacial area for droplets impact on solid surfaces

P. Xie[a,c], H. Ding[a,b], D.B. Ingham[a], L. Ma[a,*], M. Pourkashanian[a]

[a] Energy 2050, Department of Mechanical Engineering, Faculty of Engineering, University of Sheffield, Sheffield S10 2TN, UK

[b] Tianjin Key Laboratory of Process Measurement and Control, School of Electrical and Information Engineering, Tianjin University, Tianjin 300072, China

[c] Global Energy Interconnection Research Institute Europe GmbH, Berlin 10623, Germany

[*]Corresponding author:

E-Mail: lin.ma@sheffield.ac.uk (L. Ma)

Highlights

- The interfacial areas of droplets during impact on solid surfaces are analysed.
- A new correlation for predicting the maximum gas-liquid interfacial area is proposed.
- The dynamic contact angle with local grid refinement is implemented in the CFD model.
- The impact of droplets on both hydrophobic and hydrophilic surfaces are studied.
- The inner flow field of droplets during impact onto a solid surface is described.

Abstract

A better understanding of the variation of the gas-liquid interfacial area during droplets impact on solid surfaces in detail is extremely important for process intensification since this can lead to a much-increased efficiency of the heat and mass transfer. At present, experimental observation is the most popular method to investigate the droplet behaviours during the impact of the droplet. However, it is difficult to measure the interfacial areas and observe the transient inner flow field in the droplet. The CFD with VOF model is a powerful and efficient tool for investigating the visual dynamic behaviours, interfacial areas and the detailed inner flow field of droplets. Therefore, effective and efficient CFD

models are established to investigate the droplet impact onto solid surfaces through using the VOF model with dynamic contact angle and local grid refinement techniques. The CFD predictions of the dynamic behaviours of the droplets are in reasonable agreement with experimental data over a wide range of surface and liquid properties. The simulation results showed that the gas-liquid interfacial area decreases slightly at the kinematic stage, then increases at the spreading stage, and reaches its maximum at the end of the spreading stage. The hydrophilic surface promotes the increase of gas-liquid interfacial area through releasing the liquid-solid interface energy, while the hydrophobic surface promotes the increase of the gas-liquid interfacial area by promoting droplet breakup. Finally, the energy conversion of the droplet impact on the solid surface is analysed, and a new correlation for predicting the maximum gas-liquid interfacial area of the droplet is proposed.

Keywords

Drop impact; Interfacial area; Dynamic contact angle; Dynamic local grid refinement; Process intensification

1. Introduction

Droplet impact onto solid surfaces is a popular phenomenon in many industrial processes, including rapid spray cooling of hot surfaces [1-3], spray and jet reactors [4, 5], fuel injection and combustion [6, 7], metal soldering and additive manufacturing [8, 9], etc. In these applications, the interphase heat and mass transfer occur through the corresponding phase interface; therefore, increasing the interfacial area is an effective way to enhance the interphase heat and mass transfer. In the process of a droplet normal impact on a solid surface, the increase of gas-liquid interfacial area is mainly realized by two modes: (i) Extend the surface of a droplet by the large deformation of the droplet. This is because the surface area of a sphere is the smallest for the same volume liquid, as it changes from a sphere to another shape, the interface area increases; (ii) Extend the surface of a droplet by droplet breakup. The specific surface area of a spherical droplet is $6/D$, where D is the diameter of the droplet, therefore, a big droplet breakup into small droplets can increase the specific surface area of the droplet. Accurate prediction and control of the interfacial area of droplets are crucial for optimizing the relevant industrial processes. At present,

the impact behaviour of droplets on solid surfaces has been extensively studied, as discussed in several reviews [10-13]. Among the investigations, the spreading dynamics and the splashing dynamics of droplets are two important aspects. For the spreading of droplets, many efforts have been made to understand the changes in droplet diameter and predict the maximum spreading diameter of droplets. A series of experiments have been designed for observing and measuring the dynamic behaviours of droplets with different substrates [14-16]. However, very few studies have focused on the change in the area of the gas-liquid interface when the droplet impacts on a solid surface, mainly because it is difficult to measure accurately.

As a supplement to the experimental techniques, CFD technology has the potential to obtain more detailed information on the behaviour of droplets. Different numerical schemes have been developed to track or capture the gas-liquid interface, such as level set methods, volume of fluid (VOF) methods, front tracking methods, and phase-field methods, etc. Since the VOF model is naturally volume-conserved, it has been popular for investigating the droplet impact dynamics [17-26]. When simulating a droplet hitting a surface, the proper treatment of the moving three-phase (gas-liquid-solid) contact line is very important for improving the simulation accuracy, and it is usually modelled by imposing a contact angle. Since we are interested in the macroscopic motion of droplets, it is efficient to resolve only this part of the flow through embedding an apparent contact angle model [27, 28]. The simplest apparent dynamic contact angle model is the advancing–receding contact angle model, where the fixed static advancing or receding contact angle is set to a boundary condition when the contact line spreads or recoils [29, 30]. Further, several empirical formulas of the apparent dynamic contact angle as a function of the contact line velocity and the prescribed static or dynamic contact angle have been proposed [24, 31-34]. Among them, the Kistler model [32] is easy to be implement and it has shown the ability to reproduce the experimental results accurately. In addition, Malgarinos et al. [35] implemented a wetting force model [36] in VOF simulations, which can overcome the need of a pre-defined dynamic contact angle law for the cases of low Weber number impacts. In order to accurately predict the movement of the three-phase contact line and obtain a high-resolution gas-liquid interface, these regions need very fine grids. However, it is very expensive to use a uniform fine grid considering the required calculation time and computational resource. Thus, adaptive grid refinement technologies should be

used. Theodorakakos and Bergeles [37] proposed a multi-level dynamic local grid refinement method, which refines the cells that within a prescribed distance from the interface, and Malgarinos et al. [35, 38] proposed and tested a new wetting force model and an interface sharpening scheme using the dynamic local refined grid. Also, Jian et al. [39] numerically investigated the droplet splashing mechanism when it impacts on a solid substrate by using a dynamic local grid refinement method. However, these researches are only performed in 2D simulations, which cannot capture the non-axisymmetrical fierce crash of droplets. Recently, Cimpeanu and Papageorgiou [40] investigated 3D high-speed droplets impact onto solid surfaces at arbitrary angles using VOF model with dynamic local grid refinement. This method allows detailed study of droplet morphology ranging from tens to hundreds of microns, which proves the power of the modelling method used. Similarly, accurately reproduce the dynamic behaviour of the droplet and track the change of the interface area through CFD simulations could be a good way to study the change of the interface area when a droplet impacts on a solid surface.

In addition to CFD simulations, it is more efficient to use a mathematical model to predict the maximum gas-liquid interfacial area of a droplet when it impacts on a solid surface. At present, it is estimated mainly by approximating the shape of the droplet at maximum spread. Different shape approximations have been proposed, such as cylindrical disk [14, 41-45], spherical cap [46], ring-like shape [47], harmonic average of a spherical cap and a cylindrical disk [48], rim-lamella shape [49], etc. The prediction accuracy of these models depends on the similarity between the approximate shape and the real shape [49]. In addition to the shape approximation methods, the maximum gas-liquid interfacial area can be obtained through energy conservation analysis. The accuracy of this method depends on the calculation of each energy component during droplet impact, especially the prediction of the energy dissipation. It is worth mentioning that both of the two methods require the maximum spread factor of the droplet, and different correlations have been established for predicting the maximum spread factor based on different approaches, including momentum conservation [50], scaling analysis [51, 52] and energetic analysis [14, 41-45, 48, 49, 53].

This paper focuses on the analysis and prediction of the gas-liquid interfacial area for droplets impacting on solid surfaces through CFD simulation and energetic analysis. The structure of this paper is organised as follows: Section 2 describes the CFD modelling method of droplet hits a solid surface.

Both the 2D axisymmetric and 3D CFD models using the VOF method with the dynamic contact angle model and the local grid refinement techniques have been built to accurately capture the gas-liquid interface and the moving contact line. In Section 3, the spread factor, interfacial area and inner flow field of droplets in different impinging regimes with different liquid properties and surface properties are analysed and discussed. Then, in Section 4, a correlation for predicting the maximum gas-liquid interfacial area of a droplet is proposed based on the energetic analysis. Finally, conclusions are presented in Section 5.

2. CFD simulation

2.1. The governing equations

In order to track the interface accurately, the VOF model proposed by Hirt and Nichols [54] is used. Both the gas and liquid phases are assumed to be incompressible, then the conservation equations for mass and momentum and the transport equation for the volume fraction are as follows:

$$\nabla \cdot \vec{u} = 0 \tag{1}$$

$$\frac{\partial}{\partial t}\left(\rho\vec{u}\right) + \nabla \cdot \left(\rho\vec{u}\vec{u}\right) = -\nabla p + \nabla \cdot \left[\mu\left(\nabla\vec{u} + \nabla\vec{u^T}\right)\right] + \rho\vec{g} + f_{vol} \tag{2}$$

$$\frac{\partial \alpha_L}{\partial t} + \vec{u} \cdot \nabla\alpha_L = 0 \tag{3}$$

where $\vec{g}$ is the gravitational acceleration, f_{vol} is the source term considering the effect of surface tension. The fluid properties are the volume-averaged values, as follows:

$$\rho = \alpha_L\rho_L + (1-\alpha_L)\rho_G \tag{4}$$

$$\mu = \alpha_L\mu_L + (1-\alpha_L)\mu_G \tag{5}$$

Brackbill et al. [55] used the CSF model to convert the surface tension into the body force, and it is expressed as:

$$f_{vol} = \sigma_{GL}\kappa\nabla\alpha_L\frac{\rho}{\frac{1}{2}(\rho_L+\rho_G)} \tag{6}$$

where σ_{GL} is the surface tension coefficient, κ is the surface curvature, and it is defined in terms of the divergence of the unit normal:

$$\kappa = -\nabla \cdot \vec{n}, \quad \vec{n} = \frac{\nabla \alpha_L}{|\nabla \alpha_L|} \tag{7}$$

where $\nabla \alpha_L$ is the gradient of the volume fraction of liquid.

The surface normal at the wall-adjacent cell is expressed as:

$$\vec{n} = n_w \cos\theta_d + t_w \sin\theta_d \tag{8}$$

where n_w and t_w are the unit vectors normal and tangential to the wall, respectively, and θ_d is the contact angle at the wall.

The Kistler's dynamic contact angle model [32] and the wetting force model (WFM) [35] were employed for specifying the contact angle at the wall θ_d. For the Kistler's model, the apparent dynamic contact angle is given as a function of the capillary number and the inverse of Hoffman's function:

$$\theta_d = f_H\left(Ca + f_H^{-1}(\theta_e)\right) \tag{9}$$

where f_H^{-1} is the inverse function of Hoffman's function:

$$f_H(x) = \arccos\left\{1 - 2\tanh\left[5.16\left(\frac{x}{1+1.31x^{0.99}}\right)^{0.706}\right]\right\} \tag{10}$$

where $x = Ca + f_H^{-1}(\theta_e)$, and $\mathrm{Ca} = \mu_L u_{cl}/\sigma_{GL}$. Most surfaces are not smooth and are subject to the effect of contact angle hysteresis, thus the equilibrium contact angle θ_e is replaced by either the quasi-static advancing contact angle θ_{adv} or the quasi-static receding contact angle θ_{rec} based on the sign of the contact line velocity vector [23].

The contact line velocity is calculated from the actual velocity at cells:

$$\vec{u_{cl}} = (u_{cell} \cdot n_t)\frac{n_t}{|n_t|} \tag{11}$$

The contact line direction is calculated by:

$$sign = \vec{u_{cl}} \cdot \vec{n} \tag{12}$$

If *sign* is positive, then the contact line is receding. If *sign* is negative, the contact line is advancing.

2.2. Dynamic local grid refinement

Level-set method is a popular interface-tracking method for simulating two-phase flows with topologically complex interfaces [56], and the distance from the gas-liquid interface predicted by the level-set method can be used as the criteria to refine the grids near the interface. The level-set function (LSF) φ is defined as a signed distance to the interface, and the φ evolution can be given by:

$$\frac{\partial \varphi}{\partial t} + \nabla \cdot \left(\vec{u}\varphi\right) = 0 \tag{13}$$

where the interface is the zero-level set, and $\varphi(x, t)$ can be expressed as:

$$\varphi(x,t) = \begin{cases} +|d| & \text{if } x \in \text{the primary phase} \\ 0 & \text{if } x \in \text{the interface} \\ -|d| & \text{if } x \in \text{the secondary phase} \end{cases} \tag{14}$$

where d is the distance from the interface.

In order to increase the calculation efficiency, the dynamic grid refinement region is restricted to a certain region that is close to the gas-liquid interface. For the 2D axisymmetric domain, the refinement region is within $0.2D_0$ to the interface, namely $-0.2D_0 \le \varphi \le 0.2D_0$; for the 3D domain, the refinement region is within $0.1D_0$ to the interface, namely $-0.1D_0 \le \varphi \le 0.1D_0$. The level of refinement for a region depends on its distance to the interface, and the different refinement regions are marked using the level-set function φ. For example, the refined 2D axisymmetric domain is expressed as follows:

$$Level = \begin{cases} 4 & \text{if} \quad |\varphi| \le \dfrac{0.2D_0}{8} \\ 3 & \text{if} \quad \dfrac{0.2D_0}{8} < |\varphi| \le \dfrac{0.2D_0}{4} \\ 2 & \text{if} \quad \dfrac{0.2D_0}{4} < |\varphi| \le \dfrac{0.2D_0}{2} \\ 1 & \text{if} \quad \dfrac{0.2D_0}{2} < |\varphi| \le 0.2D_0 \\ 0 & \text{if} \quad \text{others} \end{cases} \tag{15}$$

where, D_0 is the initial droplet diameter. Refined grids are produced by the method of hanging node adaption. If the current level of the cell is lower than expected level, then the cell in the 2D domain is split into 4 cells or the cell in the 3D domain is split into 8 cells. Conversely, if the current level is larger than the expected level, then this grid is made coarser.

The 60 × 60 and 80 × 80 × 80 identical coarse-level quadrilateral cells were mapped in 2D axisymmetric and 3D domains, respectively. Then, the local multi-level grid refinement around the interface was applied, as shown in Fig. 1.

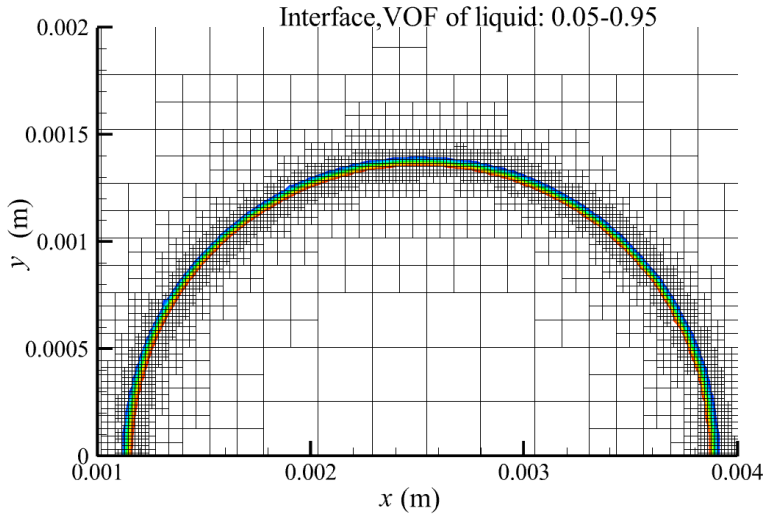

(a)

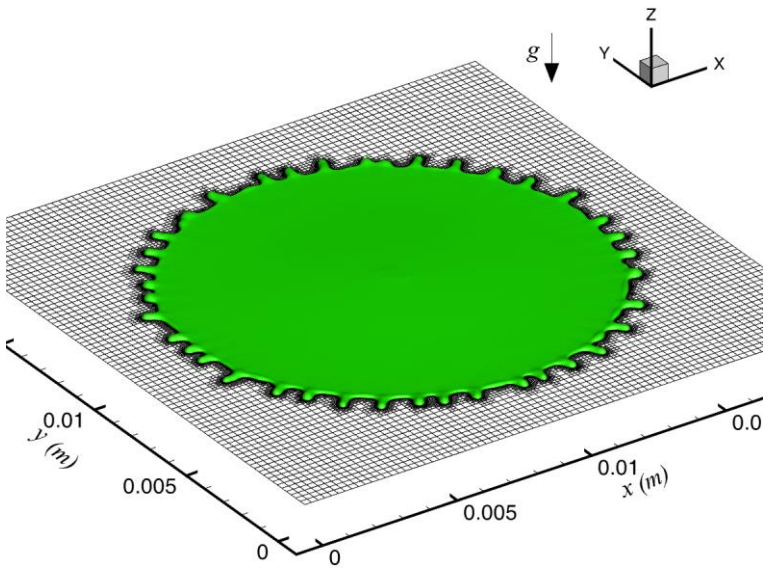

(b)

Fig. 1. Geometry, boundary conditions and grid with the dynamic local grid refinement technique. (a) eZoom of the 4-level of local grid refinement and the interface details of the 2D model, and (b) the 4-level of the local refinement grid for the 3D model (only 3-levels shown).

For a 2D domain, it is found that the differences in the temporal evolutions of the spreading ratio between the 4-level and 5-level refined grid is less than 2% which means that the 4-level refinement can achieve a grid independent solution. Using this technique, the number of the cells can be reduced by 100 times compared with a uniform refined grid using the same grid resolution in the whole computational domain. In addition, the minimum cell size around the interface is about 15 μm which means there are more than 400 nodes on the 2D circumference of the initial droplet. For a 3D domain,

a 4-level refined grid can achieve a grid independent solution for the different cases. The minimum cell size around the interface is about 15 μm, and more than 120,000 nodes are employed on the sphere of the initial droplet with a diameter of 3.0 mm. In addition, the number of the dynamic local refined cells varies from 0.8 to 8.0 million, whereas the number of cells is 2,097 million for the whole-domain with a uniform 4-level refined grid. In this study, for the purpose of saving computing time, this new local refined grid is only created every 20 time steps.

2.3. Boundary conditions and numerical schemes

For the droplet normal impact onto a dry solid surface, the axisymmetric pattern was simulated in the 2D axisymmetric computational domain for the purpose of saving grids, and the non-axisymmetric pattern was simulated in the 3D computational domain. In this study, the ranges of the initial velocity and diameter of the droplets are 0.85 - 4.1 ms^{-1} and 2.28 - 3.17 mm, respectively. Further, the maximum spread diameter is less than 6 times that of the initial diameter. Thus, the computational domains are set to be 15 mm × 15 mm for the 2D axisymmetric model and 20 mm × 20 mm × 20 mm for the 3D model. The initial condition in the computational domain is a spherical droplet with a uniform velocity where the initial distance from the centre of the droplet to the wall is equal to its diameter. For the 2D model, one of the vertical boundaries is set to be the axisymmetric boundary. For the 3D model, the droplet is located at the middle of the *x*-*y* plane. The wall is a no slip stationary boundary and the wall adhesion is specified by dynamic contact angle model. The other lines or faces in the computational domain are set to be the pressure-outlet boundary, and the static pressure is specific as 0 Pa.

The PISO algorithm was used to solve the transient pressure and velocity coupling, the body force weighted discretization was used for the pressure equation, and a second-order upwind scheme was adopted for the momentum equations. The Geo-Reconstruct scheme was employed for tracking the gas-liquid interface. Both the level-set functions and the transient schemes were solved using the first-order upwind scheme, and all the nonlinear equations were linearized and solved using the algebraic multigrid method [57]. The volume fraction was calculated using the explicit scheme, and the time steps of 0.05 μs, 0.2 μs, 0.5 μs and 2.0 μs have been chosen to test the time step independence, and 0.5 μs was regarded as the suitable time step size considering both the accuracy and the computational speed. The

criterion of convergence is that the residuals of all equations are less than 10^{-4}. The gas-liquid interfacial area A_{GL} was calculated through integrating the gas-liquid interfacial area in each gas-liquid boundary cell. In order to eliminate the error at the liquid-solid interface, $\alpha_L = 0.1$ was regarded as the gas-liquid interface.

2.4. Case descriptions

Eight representative cases [14-16, 22-24] were selected for performing the simulations. The selected experimental cases have detailed experimental conditions, including liquid properties, surface properties and contact angle parameters, as well as clear figures and quantitative results. In addition, in order to verify the adaptability of the established CFD model, the selected parameters of experimental conditions cover a wide range. The important parameters of these cases are presented in Table 1, and the fluid properties of the employed liquid and gas phases are listed in Table 2. In Table 1, u_0 is the initial velocity of the droplet, D_0 is the initial diameter of the droplet, θ_{adv} and θ_{rec} are the quasi-static advancing and receding contact angles, respectively. If they were not given in literature, they were assumed equal to the static contact angle. *We* is the Weber number, which was calculated by $We=\rho u_0^2 D_0/\sigma$. *Re* is the Reynolds number, which was calculated by $\mathrm{Re}=u_0 D_0 \rho/\mu$. *Oh* is the Ohnesorge number, which represents a dimensionless number that relates the viscous forces to the inertial and surface tension forces, $Oh = \mu/\sqrt{\rho\sigma D_0} = \sqrt{We}/Re$.

Table 1 Parameters employed in the simulation cases.

No.	Liquid/Wall	u_0 (m/s)	D_0 (mm)	θ_{adv} (°)	θ_{rec} (°)	*We*	*Re*	*Oh*	Ref.
Case 1	Water/Wax	1.18	2.75	105	95	52.3	3,238.5	0.00223	Rioboo [15]
Case 2	Water/Wax	0.85	2.70	97	97	26.7	2,290.4	0.00225	Mao [14]
Case 3	Water/Silicon	1.0	2.28	114	64	31.2	2,275.4	0.00245	Yokoi [24]
Case 4	Water/Glass	1.17	2.7	10	6	50.5	3152.7	0.00225	Šikalo [16]
Case 5	Glycerin/Wax	4.1	2.45	97	90	797.5	105.6	0.26732	Šikalo [23]
Case 6	Glycerin/Wax	1.41	2.45	97	90	94.3	36.3	0.26732	Šikalo [23]
Case 7	Water/Wax	3.6	3.17	105	95	561.7	11,389.2	0.00208	Rioboo [15]
Case 8	Tin/Steel	3.0	2.7	140	140	322.3	29,504.1	0.00061	Bussmann [22]

Table 2 Properties of the liquids and gas that were used in the simulations.

Liquid/Gas	σ (N m^{-1})	μ (mPa.s)	ρ (kg m^{-3})	*Ca* at u_{cl} =1 m s^{-1}
Water	0.073	1.0	998	0.0137
Glycerin	0.063	116	1220	1.841
molten tin	0.530	1.93	7030	0.0036
Air	-	0.0179	1.225	-

Upon considering all the simulated cases, the contact angle is within the range of 6° - 140°, the Weber number is within the range of 26.7 - 797.5, and the Reynolds number is within the range of 36.3 - 29,504.1. Specifically, Case 1 - 3 are concerned with the water droplet impact on hydrophobic surfaces. Case 4 is about the impact of a water droplet on a hydrophilic surface. Case 5 and 6 refer to the glycerin droplet impact on hydrophobic surfaces, where the glycerin has a higher viscosity than water, and therefore this results in a bigger value of the Ohnesorge number *Oh* and the capillary number *Ca.* In addition, Case 7 and 8 are about the water and molten tin droplets impact on hydrophobic surfaces with high *Re* numbers, which result in non-axisymmetric patterns, therefore they were simulated using 3D models.

3. Simulation results and discussion

3.1. The impact of water droplets on hydrophobic surface

3.1.1. The droplet dynamics and 2D axisymmetric model validation

Water droplets impacting hydrophobic surfaces is a typical process in many applications [58-60]. Accurately reproducing the dynamic impact process through CFD simulation is very important for analysing their detailed behaviours. Comparisons of the simulation and the experimental results of Cases 1-3 are shown in Fig. 2. It shows that the simulated spatial-temporal evolutions of the spread, recoil, rebound and breakup behaviours are in good agreement with the experimental results [14, 15, 24]. The time evolution of the impact process can be divided into four stages: the kinematic, spreading, relaxation and wetting/equilibrium stages. At the kinematic stage, the droplet is like a truncated sphere, and no lamella forms and spreads. With the increase of time, the droplet begins to spread, and it is governed by

250 inertia. At the same time, the surface tension and viscosity combine to damp the droplet spreading, and
251 a rim of the spreading lamella appears at the edge of the spreading droplet film. At the end of the
252 spreading stage, the droplet reaches its maximum spreading. Then, the gas-liquid-solid contact line of
253 the droplet begins to recede, and this is called the relaxation stage, where the surface tension minimizes
254 the gas-liquid interface of the droplet. Take Case 1 as an example, during the relaxation stage, the droplet
255 goes from a pancake shape (at t = 6.02 ms, t^* = 2.58) to a truncated sphere on the hydrophobic surface
256 (at t = 10.26 ms, t^* = 4.40), as shown in Fig. 2 (a). Then, depending on different kinetic energies
257 contained, there are different movement regimes. If the droplet contains sufficient kinetic energy, then
258 part of the droplet can bounce back from the solid surface as shown in Fig. 2 (a) and (b). Otherwise it
259 sticks to the surface and reaches equilibrium after several oscillations, as shown in Fig. 2 (c).

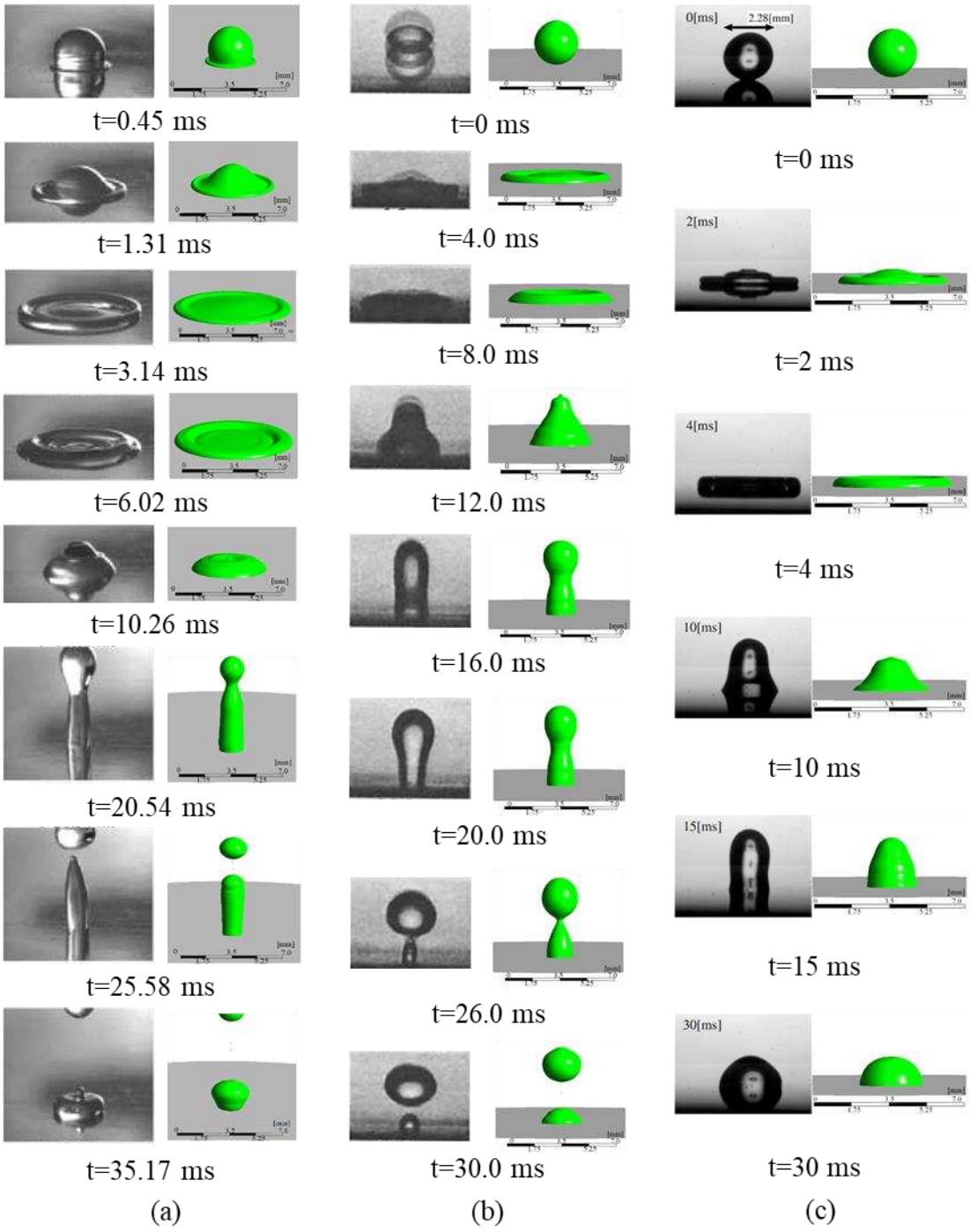

Fig. 2. Experimental and CFD simulation results of the dynamic droplets during the spreading, recoiling and bouncing regimes: (a) Case 1, based on Rioboo et al. [15], (b) Case 2, based on Mao et al. [14], and (c) Case 3, based on Yokoi et al. [24].

The spread factor D^* is defined as D/D_0, where D is the diameter of the liquid-solid contact interface, and D_0 is the initial droplet diameter. For a further validation of the 2D axisymmetric model, the time evolution of the spread factor D^* in Case 1 is presented in Fig. 3. The development stages of D^* matched well with the experimental measurements [15] when employing the Kistler model [32] or

the wetting force model (WFM) [36]. The simulated maximum spread factor D_m^* is 2.96 with the Kistler model and 2.69 with the WFM method, and the experimental result is 2.62. The difference between the simulated maximum spread factor D_m^* and the experimental measured D_m^* is within 13%, which indicates that the 2D axisymmetric CFD model is acceptable for investigating the detailed behaviour of the droplet impact. Since the Kistler model is more robust for simulating the impact at different conditions, it was used to produce the CFD results in this paper. In addition, the time evolution of the dynamic contact angle when employing the Kistler model is plotted in Fig. 3, and the values of the experimental measured advancing contact angle θ_{adv} and receding contact angle θ_{rec} are also marked in the figure. An interaction between the fluid viscosity, the surface tension, the inertia and the substrate leads to the real-time dynamic contact angle θ_d being a function of the velocity of the contact line u_{cl}, which is very important for reproducing the dynamic impact process in the simulation [61].

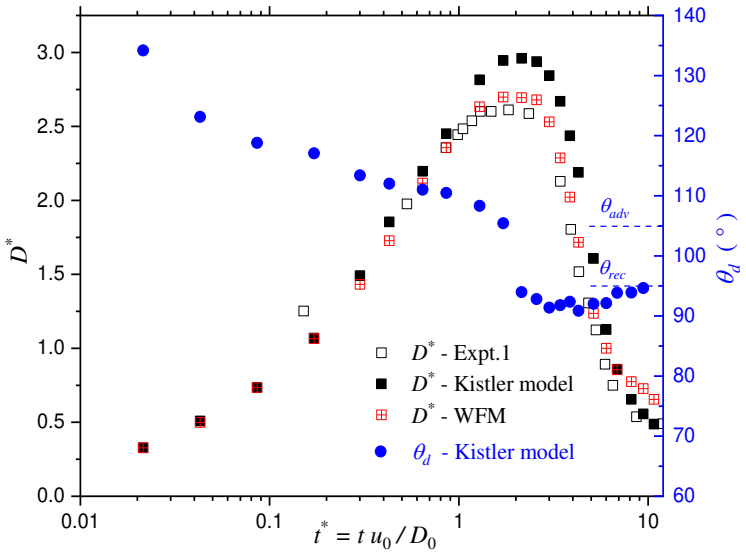

Fig. 3. Time evolutions of the spread factor of a water droplet and the dynamic contact angle in Case 1 using both the Kistler model [32] and the wetting force model (WFM) [36] for the hydrophobic surface.

3.1.2. Variations of the interfacial areas

The interfacial areas are crucial parameters for affecting the interface heat and mass transfer. In order to analyse and compare the variations of the gas-liquid interfacial area and the solid-liquid interfacial area in different impact regimes, two interfacial area factors were proposed. (i) The gas-liquid interfacial area factor A_{GL}* is defined as A_{GL}* =A_{GL}/A_{GL0}, where A_{GL} is the real-time gas-liquid interfacial area and A_{GL0} is the initial gas-liquid interfacial area of the spherical droplet; (ii) The solid-liquid

interfacial area factor A_{SL}* is defined as A_{SL}* =A_{SL}/A_{GL0}, where A_{SL} is the real-time solid-liquid interfacial area. Variations of A_{GL}*, A_{SL}* and the spread factor D^* of the droplets in Case 1–3 are presented in Fig. 4.

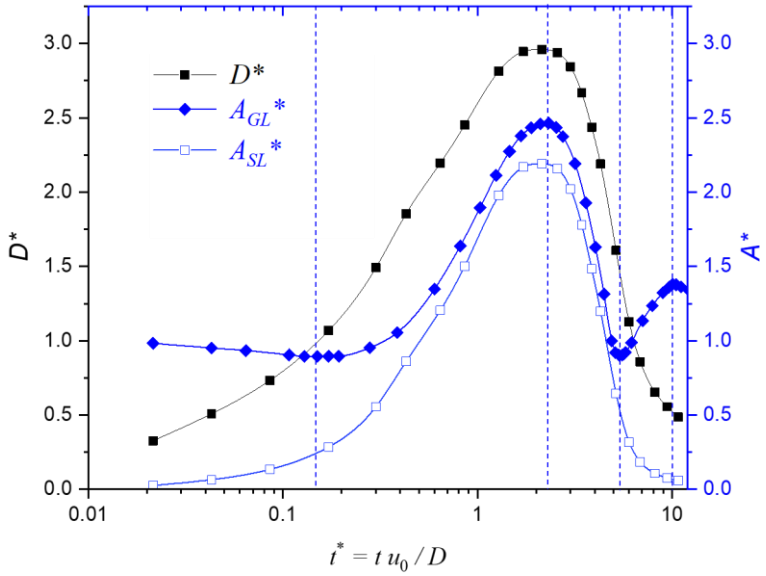

(a)

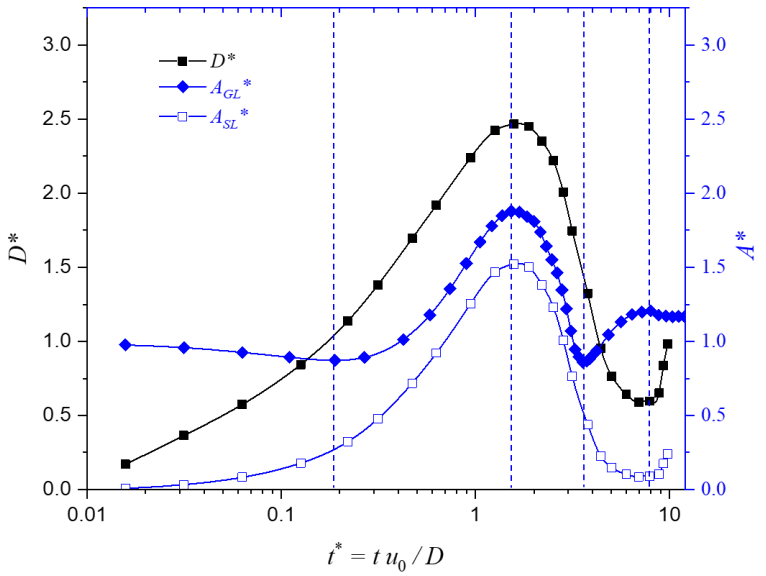

(b)

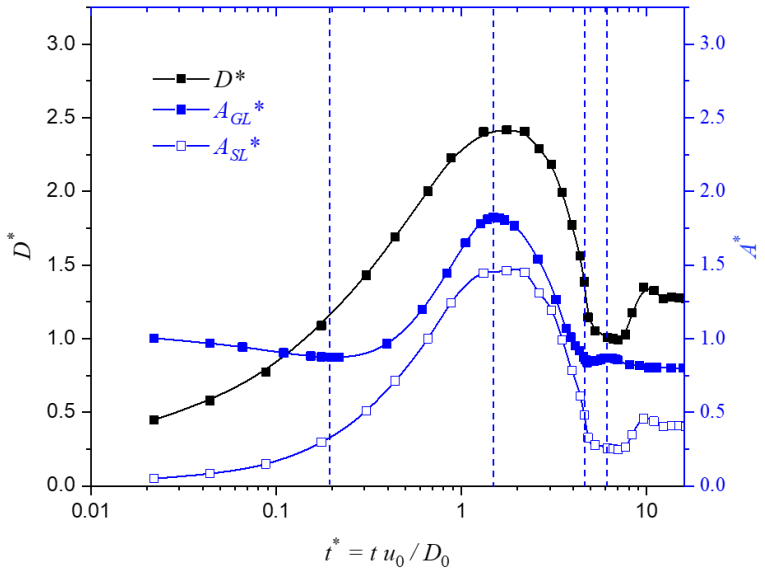

Fig. 4. Variation of the spread factor and gas-liquid interfacial area factor: (a) Case 1, based on Rioboo et al. [15], (b) Case 2, based on Mao et al. [14], and (c) Case 3, based on Yokoi et al. [24].

As shown in Fig. 4, A_{GL}* can be divided into five stages by four changing points according to the variation of its value. Accordingly, the morphologies of the droplets at the four A_{GL}* changing points are shown in Fig. 5. From observing Fig. 4 and Fig. 5, at the kinematic stage, A_{GL}* slightly decreases due to the droplet changing from a sphere to a truncated sphere and part of the gas-liquid interface being replaced by the solid-liquid interface A_{SL}. Then, at the spreading stage, the gas-liquid interfacial area increases with the shape of the droplet changing from the truncated sphere to the lamella, and the increase of the gas-liquid interfacial area keeps pace with the increasing of the droplet diameter. At the end of the spreading stage, the D*, A_{GL}* and A_{SL}* almost reach their maximum value at the same time, and the A_{GLm}* (maximum A_{GL}*) of Cases 1-3 are 2.47, 1.88 and 1.82, respectively. Then, the gas-liquid-solid contact line begin to recede under the action of surface tension, and the regained kinetic energy makes the droplet rebound. During the rebound process, A_{GL}* first decreases to its minimum value, then it increases with the longitudinal stretch of the droplet. When A_{GL}* decreases to its minimum value, the droplet is similar to a conical shape as shown in Fig. 5. Before it reaches its minimum value, the surface tension acts as a driving force for the drop rebound, while with the increase of A_{GL}*, it becomes a resistance for the droplet prolonging. If the droplet has a tall rebound, then the surface tension can shrink the prolonged liquid column and squeeze out a small droplet at the top of the liquid column, as shown in Fig. 5 (a) and (b). Before the droplet separate from the liquid column, the gas-liquid interfacial area

reaches its second extremum. Then, the gas-liquid interfacial area decreases and oscillates before the droplet reaches a balanced state. Looking at the whole process, it can be found that D^* and A_{GL}^* have different variation trends, which means the variation of the gas-liquid interfacial area A_{GL} cannot be simply represented by the variation of the droplet diameter. Comparing Fig. 4 (a) and (b), it can be found that with a higher impact velocity, A_m^* becomes bigger, which is one of the ways for process intensification.

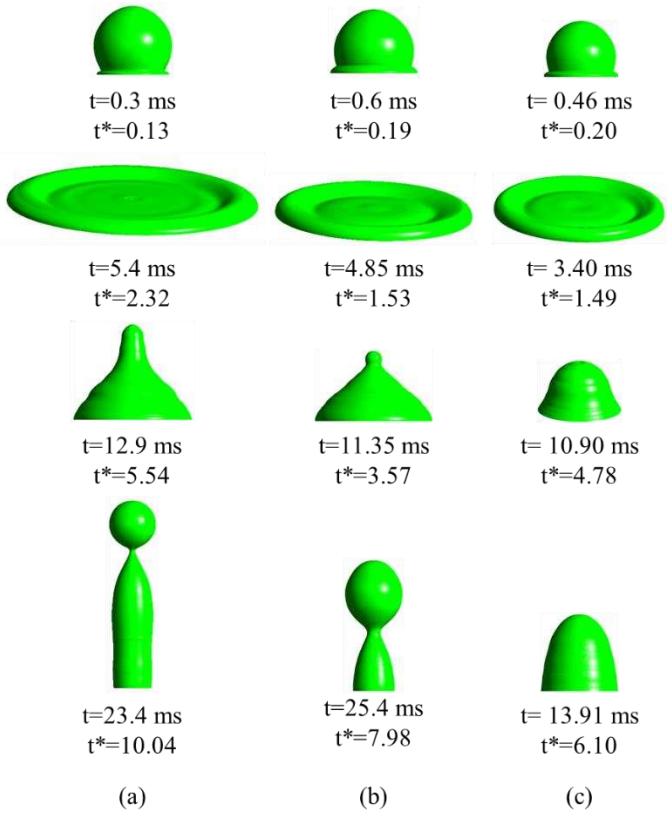

Fig. 5. Morphologies of the droplets at the A_{GL}^* changing points shown in Fig. 4: (a) Case 1, (b) Case 2, and (c) Case 3.

3.1.3. *Inner flow field of the droplet during impact*

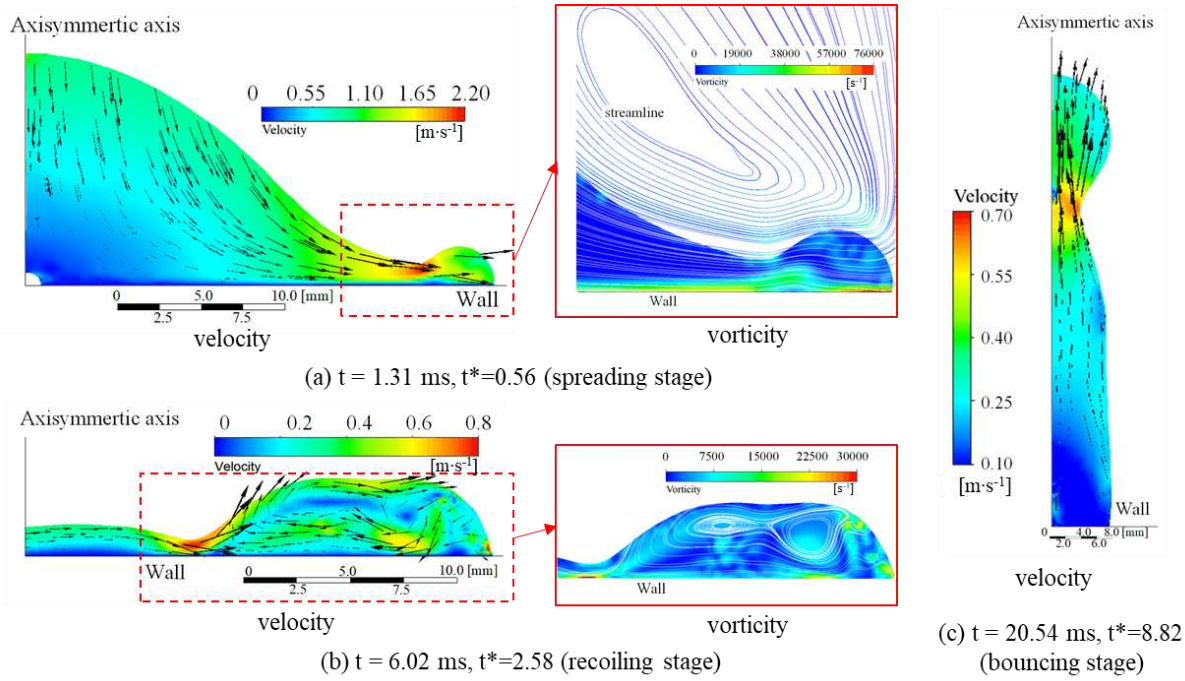

Fig. 6. The velocity vector and the vorticity distribution of the droplet during spreading, recoiling and bouncing regimes in Case 1.

Parameters of the droplet inner flow field, such as the velocity vector, the vorticity distribution and the thickness of the boundary layer, significantly affect the calculation of viscous dissipation in the droplet [41-43, 45, 48] and the interfacial heat and mass transfer [62]. However, these parameters are very difficult to be measured by experimental methods, therefore they are analysed through using the accurately reproduced results from CFD simulation. Fig. 6 shows the velocity and vorticity vertical cross-section diagrams of the droplet in Case 1 at the spreading, recoiling and bouncing regimes. At t = 1.31 ms (t* = 0.56), the droplet is in the spreading stage, as shown in Fig. 6 (a). Under the action of inertial force, the sphere is stretched into a pie disk shape, and the larger liquid surface is exposed to the gas phase. In addition, a small bubble can be observed under its centre, and a detailed explanation about this phenomenon can be seen in the literature [11]. The leading edge of the rim is unstable soon after impact, and a hemispherical ring is formed due to the solid surface being hydrophobic. The maximum velocity is located at the ring groove (in 3D view) between the truncated sphere and the hemispherical ring. As shown in the vorticity contour diagram of Fig. 6 (a), during the spreading stage, there is a thin layer with a high vorticity in the near-wall region, where the viscous dissipation mainly occurred. In this stage, there are two reasons for enhancing the interfacial heat and/or mass transfer: (i) due to the

existence of the high vorticity region, the thermal resistance of the liquid-solid interface can be significantly reduced by the strong convective heat transfer; (ii) the dramatically increased gas-liquid and liquid-solid interfaces are favourable for the interfacial heat and/or mass transfer. At t = 6.02 ms (t* = 2.58), the droplet is at the beginning of the (receding) relaxation stage, as shown in Fig. 6 (b). The liquid at the outer edge of the disk is in a recoiling motion under the action of the surface tension, while the liquid near the axisymmetric axis is still in a spreading motion. Thus, there are induced vortices inside the spreading lamella, as shown in Fig. 6 (b), and these vortices generate viscous dissipation. The small vortices near the gas-liquid interface can enhance the surface renewal, thus enhancing the interfacial heat and/or mass transfer, and the large vortices in the droplet facilitate the internal convective heat and/or mass transfer. At t = 20.54 ms (t* = 8.82), the droplet is at the bouncing stage, as shown in Fig. 6 (c). The inertia overcomes the gravity and makes the droplet rebound from the wall. Under the action of surface tension, the inherent instability of the liquid column leads to the appearance of thin necks, where the velocity is maximum, and the liquid column may break into two or more small droplets. The breakup stage is investigated by the results obtained in Case 2.

In the rebound and breakup stages, the velocity vectors and vorticity distribution of the liquid phase of Case 2 are plotted in Fig. 7. At the beginning of the breakup, as shown in Fig. 7(a), a neck is found connecting the two spheres. The liquid in both the upper and lower spheres moves away from the neck, and this leads to the breakup at the narrow neck. In Fig. 7(b), these two spheres are completely broken, and the induced vortices appear inside both the two small droplets. The lower one adheres to the wall, whereas the upper one flies away. After several milliseconds, the induced vortices disappear and the upper droplet begins to fall down, as shown in Fig. 7(c). In this stage, the surface tension plays a dominant role in the droplet breakup and vortex generation.

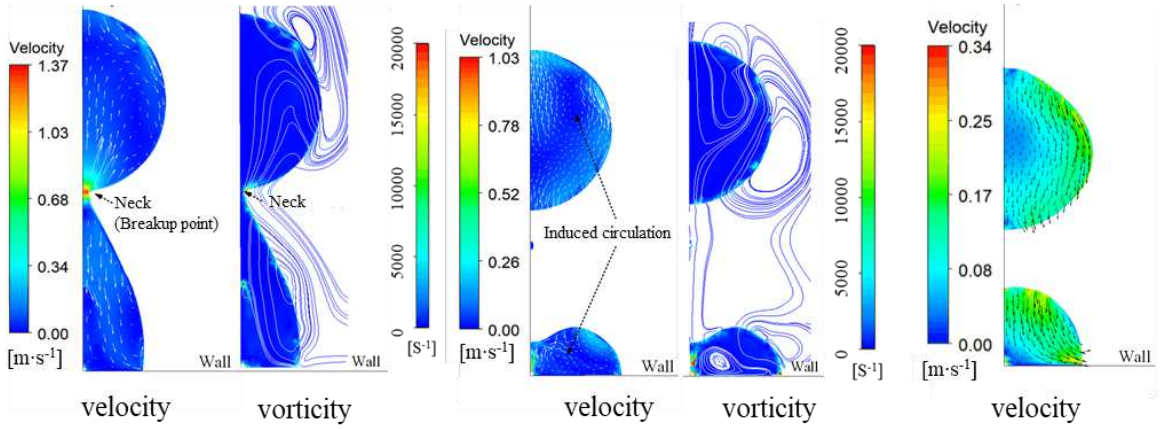

(a) t = 26.55 ms, t*=8.36 (b) t = 31.80 ms, t*=10.01 (c) t = 40.00 ms, t*=12.59

Fig. 7. The velocity, vorticity and streamlines of the droplet during the breakup regime of Case 2.

3.2. The impact of water droplet on hydrophilic surface

Case 4 is used for analysing the droplet dynamics and the variation of the interfacial areas when a droplet impacts on a hydrophilic surface. The measured θ_{adv} and θ_{rec} are 10° and 6° respectively [16], and the characteristic time t_c is equal to 2.31 ms. The time evolution of the droplet morphology is shown in Fig. 8(a), and the spread factor D^*, the gas-liquid interfacial area factor A_{GL}^* and the solid-liquid interfacial area factor A_{SL}^* of the water droplet during the impact are shown in Fig. 8(b). During the kinematic stage, the shape of the droplet changes from a sphere to a disk; the solid-liquid interfacial area keeps increasing while the gas-liquid interfacial area keeps slightly decreasing. Then, at the spreading stage, both the gas-liquid interfacial area and the solid-liquid interfacial area increases rapidly. There is no obvious recoil stage for the hydrophilic surface. Finally, the droplet enters an equilibrium state, and the A_{GL}^* and A_{SL}^* are almost identical, which means that the liquid is almost shaped like a flat film. With the diameter of the droplet increasing by 4.4 times, the gas-liquid interfacial area increases by about 4.8 times. For the hydrophilic surface, the ratio of the increased area to the increased diameter is much larger than that of the hydrophobic surface at the similar initial condition, as shown in Case 1 by Fig. 4(a). This is because the solid-liquid adhesive force is a driving force for increasing the gas-liquid interfacial area for the hydrophilic surface.

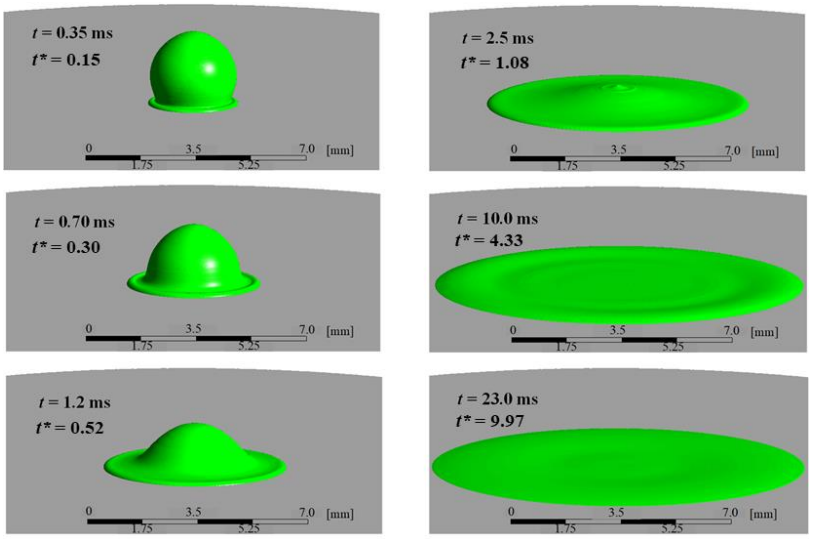

(a)

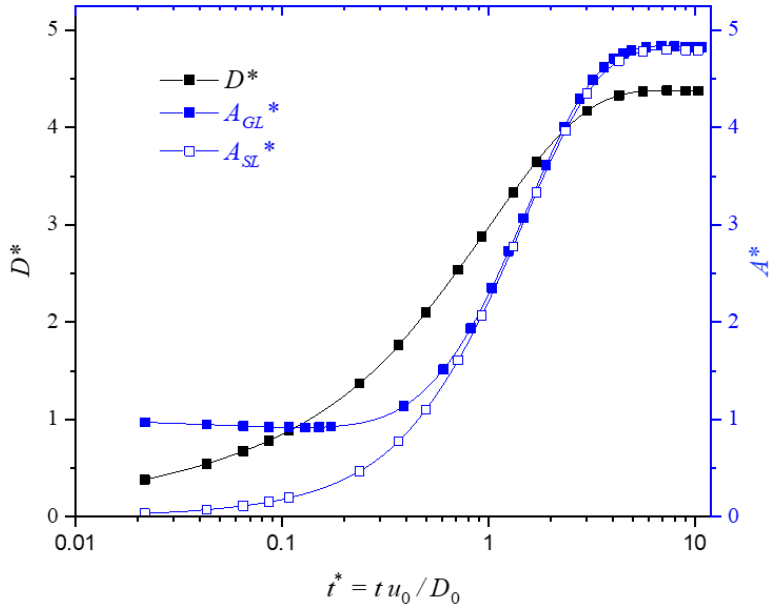

(b)

Fig. 8. (a) The time evolution of the droplet impact on a hydrophilic surface in Case 4, and (b) The time evolution of the spread factor D^*, the gas-liquid interfacial area factor A_{GL}^* and the solid-liquid interfacial area factor A_{SL}^* of the water droplet in Case 4.

3.3. The impact of a high viscous droplet on hydrophobic surface

The viscosity of the liquid phase is a crucial parameter for influencing the droplet impact dynamics and the variation of the gas-liquid interface. The impact of glycerin droplet on wax surface was investigated. Glycerin has a much higher viscosity (116 mPa.s) than water. The initial velocity was set to u_0 = 4.1 m/s and 1.41 m/s. The detailed parameters are listed in Table 1 as Cases 5 and 6. Both the simulation and the experimental results of the time evolution of the spread factor D^* and the dynamic

contact angle θ_d of Cases 5 and 6 are shown in Fig. 9(1a) and (2a). It can be seen that D^* and θ_d match well with the experiments [23], which means that the CFD model can reproduce the high viscosity droplet impact process accurately. Compared with the water droplet, the high viscosity liquid droplet has a bigger change of the dynamic contact angle θ_d during the impact. Taking Case 5 as an example, as shown in Fig. 9(1a), during the kinematic and spreading stages, θ_d is about 140°. When the droplet goes into the receding stage, θ_d decreases quickly to around 60°. This is because the high viscosity glycerin has a large viscous force, making the contact angle hysteresis more obvious than water.

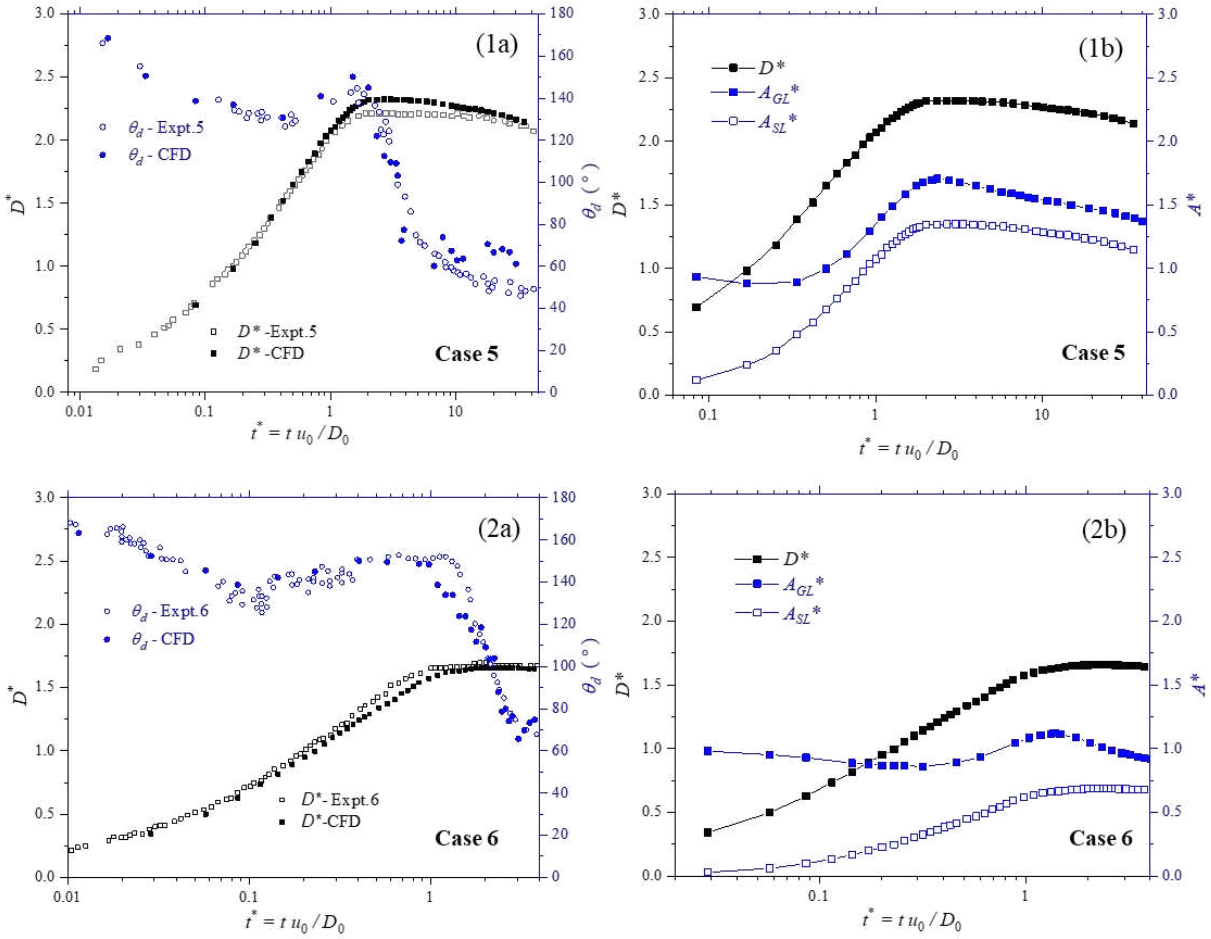

Fig. 9. Variations of spread factor D^*, the dynamic contact angle θ_d, and the interfacial area factors A_{GL}^* and A_{SL}^* in Cases 5 and 6.

The variations of A_{GL}^* and A_{SL}^* in Case 5 and Case 6 are analysed based on the simulation results, as shown in Fig. 9(1b) and (2b). After impact and before reaching the equilibrium state, the droplet oscillation is much weaker compared to water. For Case 5, as shown in Fig. 9(1b), with a high impact velocity 4.1 m/s, the maximum gas-liquid interfacial area factor A_{GLm}^* is 1.71. For Case 6, with the impact velocity at 1.41 m/s, A_{GLm}^* is 1.12, which means that the gas-liquid interfacial area only increased

slightly. For high viscosity liquids, although the impact velocity and static contact angle are both large enough, the viscous dissipation absorbs a large amount of kinetic energy, making the bounding and breakup behaviours difficult to occur. The results show that the normal impact is not a good way to increase the interface area of high viscosity liquid, while due to the obvious contact angle hysteresis, oblique impact may be a better way to stretch the droplet and increase the area of the interface.

3.4. The impact of a droplet on hydrophobic surface at a high speed

At a high impact velocity, perturbations can be observed on the rim, which can result in fingering or splashing [15, 22]. These behaviours are asymmetrical; therefore, they can only be simulated by the 3D models. Cases 7 and 8 are used to investigate the fingering and splashing, respectively, and both the experimental results and the simulation results are shown in Fig. 10. In Case 7, the impact velocity of the water droplet is 3.6 m s^{-1}, the static θ_{adv} and θ_{rec} of the water droplets on the hydrophobic wax surface are 105° and 95°, respectively, and the characteristic time t_c is equal to 0.88 ms. The flow appearance of the water droplet is shown in Fig. 10(a). During the whole impact process, no splash occurs, but the minimum film thickness is less than 50 μm. Therefore, the 4-level dynamic refined grid, which makes the minimum cell size 15 μm (1/200 of droplet diameter), is necessary for accurately simulating the 3D fingering impact process. As a result, a good agreement in the appearances between the numerical results and the experimental photographs was achieved. Several fingers appear soon after impact, and then both the size and number of the fingers gradually increase until the rim reaches its maximum spreading. The experimental and numerical D_m^* are 5.03 and 5.16, respectively. After the maximum spreading (t = 3.80 ms, t_m^* = 4.32), the surface tension force pulls the fingers back with coalescence, and eventually makes the rim recoil and bounce. It is worth noting that there is a time lag for the simulation results after 10 ms, which might be due to the effect of the roughness on the dynamic contact angle. However, the simulation results were still more accurate than the previous simulation results as shown in Ref. [63], where the non-physical splashing occurred along the circumference of the droplet after the maximum spreading.

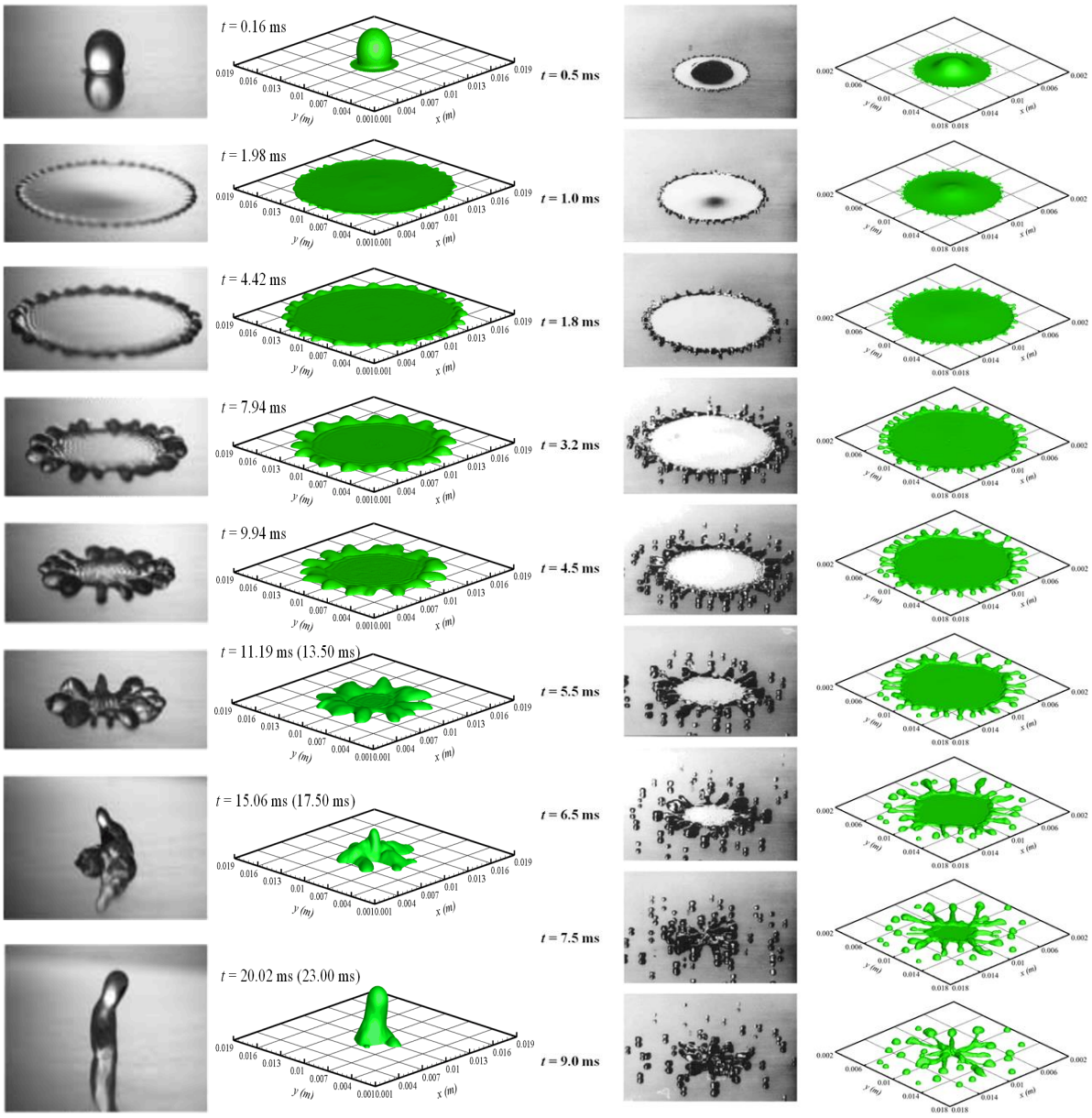

(a) (b)

Fig. 10. The simulation and experimental results for droplet impact at the fingering and splashing regime: (a) Case 7, based on Rioboo et al. [15], and (b) Case 8, based on Bussmann et al. [22].

The flow appearance of the molten tin droplet in Case 8 is shown in Fig. 10(b), where the molten tin droplet has an initial velocity of 3.0 m s^{-1}, the characteristic time t_c is 0.90 ms, and the droplet reaches the maximum spread diameter at about t = 3.2 ms. The 3D velocity vectors and vorticity distributions in the liquid phase of Case 8 are plotted in Fig. 11. At t = 1.0 ms, the droplet is at the spreading stage as shown in Fig. 11 (a). Due to the instability and a higher velocity of the rim, the vorticity at the outer region is higher than that in the central region of the droplet during the spreading stage. At t = 5.5 ms, the rim begins to splash and recoil as shown in Fig. 11 (b). Then the central liquid film recoils faster

than the fingers, which leads to the pinching off of the secondary droplets. Because of their low speed, these satellite droplets tend to stay where they were cut off. At t = 9.0 ms, there is a big snowflake droplet in the central region of the computational domain, which drags the surrounding satellite droplets together to form a new core as shown in Fig. 10(b) and Fig. 11 (c).

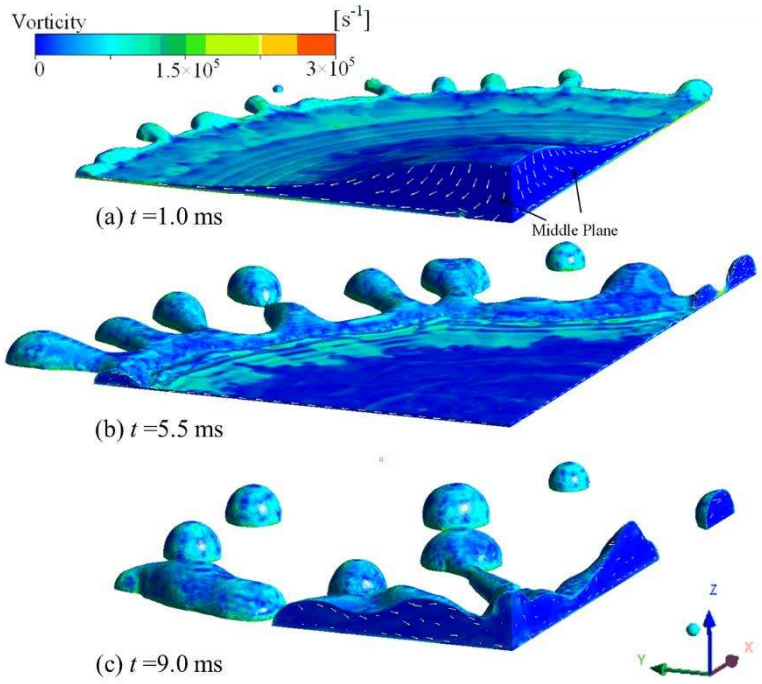

Fig. 11. The 3D velocity vectors and vorticity distributions in liquid phase during the fingering and splashing regimes in Case 8.

The variations of the gas-liquid interfacial area index A_{GL}* of Cases 7 and 8 are shown in Fig. 12. The A_{GL}* curves are similar for the two cases during the spreading stage. The A_{GL}* sharply increases, which means that the gas-liquid interfacial area is greatly increased due to the high-speed impact. Then, only one peak appears on each curve during the observing period. This is because the fingering or splashing consumes a large amount of energy, which damps the oscillation. During the receding stage, the A_{GL}* of Case 8 goes down faster than that of Case 7 due to the bigger surface tension and droplet splash. Finally, the A_{GL}* in Case 8 is bigger than that in Case 7 due to the generation of many satellite droplets. It is difficult to form a thin film with a large surface area after droplet impact on hydrophobic surfaces; therefore, promoting droplet breakup is a good choice for enhancing the gas-liquid interfacial area.

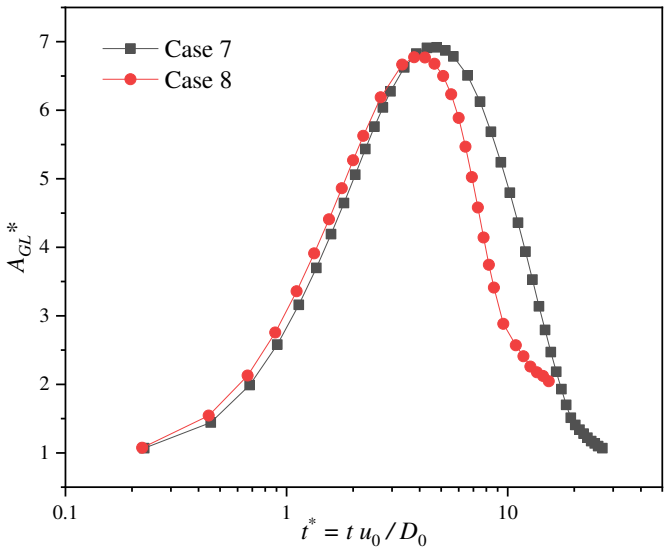

475

476 **Fig. 12**. The variations of the A_{GL}* in Cases 7 and 8.

477

478 # 4. Energetic analysis of the maximum gas-liquid interfacial area

479 ## *4.1. Derivation of the correlation*

480 As has been observed from the CFD simulation results, during the impact of droplet on solid surface,
481 the droplet has the biggest gas-liquid interfacial area almost at the end of the spreading stage. According
482 to the law of conservation of energy, the change of the total surface energy ΔE_s during the spreading
483 stage of the impact process can be expressed as follows:

$$\Delta E_s = E_k + E_P - W \tag{16}$$

484 where E_k is the initial kinetic energy of the droplet, E_P is the released potential energy, and W is the
485 energy dissipation.

486 The change of the total surface energy ΔE_s is composed of three parts, as follows:

$$\Delta E_s = \sigma_{GL}\Delta A_{GL} + \sigma_{SL}\Delta A_{SL} + \sigma_{SG}\Delta A_{SG} \tag{17}$$

487 where σ_{GL} is the interfacial energy between the gas and the liquid phase, that is, the surface tension
488 coefficient of the liquid; σ_{SL} is the interfacial energy between the solid surface and the liquid phase; σ_{SG}
489 is the interfacial energy between the solid surface and the gas phase. ΔA_{GL}, ΔA_{SL} and ΔA_{SG} are the
490 change of the gas-liquid interfacial area, the change of the solid-liquid interfacial area and the change
491 of the solid-gas interfacial area, respectively.

492 During a droplet impact on a solid surface, the increase of the solid-liquid interfacial area is equal

to the decrease of the solid-gas interfacial area, that is $\Delta A_{SL} = -\Delta A_{SG}$, therefore, ΔE_s can be expressed as follows:

$$\Delta E_s = \sigma_{GL}\Delta A_{GL} - (\sigma_{SG} - \sigma_{SL})\Delta A_{SL} \tag{18}$$

According to the Young equation [64, 65], the relationship between σ_{SG}, σ_{SL} and σ_{GL} can be expressed as follows:

$$\sigma_{SG} - \sigma_{SL} = \sigma_{GL}\cos\theta_Y \tag{19}$$

where θ_Y is the theoretical Young's contact angle, which represents solely the energetic effect of the surfaces [49].

Substituting Eq. (19) into Eq. (18), ΔE_s can be expressed as follows:

$$\Delta E_s = \sigma_{GL}(\Delta A_{GL} - \Delta A_{SL}\, cos\,\theta_Y) \tag{20}$$

In order to investigate the variation of the gas-liquid interfacial area, combining Eq.(16) and Eq. (20), ΔA_{GL} can be expressed as follows:

$$\Delta A_{GL} = \frac{E_k + E_P - W}{\sigma_{GL}} + \Delta A_{SL}\, cos\,\theta_Y \tag{21}$$

In order to resolve the value of ΔA_{GL}, the parameters on the right-hand side of Eq. (21) are calculated as follows:

(i) The initial kinetic energy E_k is calculated by

$$E_k = 0.5\rho\frac{\pi D_0^3}{6}u_0^2 \tag{22}$$

(ii) During the spreading process, the released protentional energy E_P is

$$E_P = \rho\frac{\pi D_0^3}{6}g\Delta H \tag{23}$$

where ΔH is the decreased value of the centre of mass of the droplet. At the maximum spreading state, the thickness of the droplet can be calculated by equating the volume of the spherical droplet with diameter D_0 to that of a cylinder with height h_m and diameter D_m [42], then

$$h_m = \frac{2D_0^3}{3D_m^2} \tag{24}$$

The height of the centre of mass of the droplet can be assumed to be 0.5 h_m, therefore

$$\Delta H = H_0 - \frac{D_0^3}{3D_m^2} \tag{25}$$

where H_0 is the initial height of centre of mass of the droplet, and Eq. (23) can be expressed as:

$$\Delta E_P = \rho \frac{\pi D_0^3}{6} g \left(H_0 - \frac{D_0^3}{3D_m^2} \right) \tag{26}$$

(iii) The ΔA_{SL} is the change of the solid-liquid interfacial area; before impacting, it is zero; after impacting, the solid-liquid contact area is assumed as a circular cross section; therefore, it is calculated through:

$$\Delta A_{SL} = \frac{\pi D_m^2}{4} \tag{27}$$

(iv) According to the recent research [45, 49], the dissipation work W is composed of three parts: $W = W_{vis} + W_{sp} + W_{cl}$, where W_{vis} is the viscous dissipation within the boundary layer, W_{sp} is the spontaneous dissipation associated with the "interfacial relaxation", and W_{cl} is the contact line dissipation due to the moving three-phase contact line.

The viscous dissipation W_{vis} can be calculated as follows [41]:

$$W_{vis} = \int_0^{t_m} \int_\Omega \Phi d\Omega \mathrm{dt} \approx \Phi \Omega t_m \tag{28}$$

where Φ is the viscous dissipation function, Ω is the volume where the dissipation occurs, and t_m is the elapsed time for a droplet to reach its maximum spread from the beginning of the impact. Chandra and Avedisian [41] suggested that the viscous dissipation function can be estimated by using

$$\Phi \approx \mu \left(\frac{U_c}{L_c} \right)^2 \tag{29}$$

where U_c and L_c denote the characteristic velocity and the characteristic length, respectively. Initially, Chandra and Avedisian [41] took the droplet initial velocity u_0 as U_c, the droplet height at the maximum spread h_m as L_c, and the cylindrical disk volume $\pi D_m^2 h_m/4$ as Ω. Later, Pasandideh-Fard et al. [42] modified the parameters by assuming the viscous dissipation occurs in a boundary layer with thickness $\delta = 2D_0/\sqrt{Re}$, therefore they took $L_c = \delta$, and $\Omega = \pi D_m^2 \delta/4$. Mao et al. [14] and Park et al. [46] pointed out that the boundary-layer thicknesses for low- and high- viscosity liquids need to be considered separately. For low viscosity liquids, $\delta < h_m$, it is reasonable to take $L_c = \delta$ and $\Omega =$

$\pi D_m^2\delta/4$. For high viscosity liquids, $\delta > h_m$, it is more reasonable to take $L_c = h_m$ and $\Omega = \pi D_m^2 h_m/4$ due to the viscous dissipation occurring within the whole droplet. Yonemoto and Kunugi [48] believed that the shear stress occurs in the liquid film that spreads along the solid surface, therefore they took the radial liquid velocity along the solid surface u_{R} as U_c, and they estimated that $u_{\mathrm{R}} = 3u_0/8$. From the CFD simulation results, as shown in Fig. 6 (a), for the low-viscosity fluid, the shear stress mainly exists in a thin liquid film near the wall. Therefore, we consider that it is reasonable to adopt the radial velocity u_{R} as the characteristic velocity. However, u_{R} is not a constant along the radial direction, and it changes over time in the spread stage, making it difficult to predict its value. In the vicinity of the centre of the droplet, u_{R} is smaller than the initial impact velocity u_0, but at the outer edge of the droplet, u_{R} is larger than u_0. Therefore, it is reasonable to assume that the average radial velocity of the droplet is equal to the initial velocity, that is, $u_{\mathrm{R}} = u_0$. Based on this assumption, the t_m can be estimated by $t_m = D_m/2u_R = D_m/2u_0$, which is the same as the t_m adopted by Yonemoto and Kunugi [48], Huang and Chen [45] and Wang et al. [49]. According to the above analysis, the parameters in this paper are defined as follows: $L_c = \delta$, $U_c = u_0$, $\Omega = \pi D_m^2\delta/4$, $t_m = D_m/2u_0$, where $\delta = 2D_0/\sqrt{Re}$. Therefore, the viscous dissipation is as follows:

$$W_{vis} = \frac{\pi}{16}\frac{\rho u_0^2 D_m^3}{\sqrt{Re}} \tag{30}$$

In addition, the spontaneous dissipation is as follows [45, 49]:

$$W_{sp} = \alpha\frac{\pi}{16}\frac{\rho u_c^2 D_m^3}{\sqrt{Re_c}} \tag{31}$$

where u_{c} is the critical velocity and Re_c is the associated critical Reynolds number, $Re_c = \rho D_0 u_{\mathrm{c}}/\mu$. α is the coefficient to denote the portion of the whole spontaneous dissipation. For $u_0 < u_{\mathrm{c}}$, $\alpha = 1$; for $u_0 \geq u_{\mathrm{c}}$, $\alpha = u_{\mathrm{c}}/u_0$. The u_{c} can be estimated through [45]:

$$u_{\mathrm{c}} = \left\{\frac{4\sigma_{GL}}{(\rho\mu D_0)^{0.5}\beta_{sph}}\left[\frac{4}{\beta_{sph}^2} - 2\left(1-\cos\theta_{D_m}\right) + cos\,\theta_{D_m} sin^2\theta_{D_m}\right]\right\}^{2/3} \tag{32}$$

where $\beta_{sph} = \left(4/\left(2 - 3cos\,\theta_{D_m}\,sin^2\,\theta_{D_m} - 2cos^3\theta_{D_m}\right)\right)^{1/3}$, θ_{D_m} is the apparent contact angle at the maximum spread. Because θ_{D_m} is difficult to measure and the θ_{D_m} is very close to the advancing contact

angle θ_{adv} for many surfaces as shown in [49], θ_{D_m} is assumed to equal to θ_{adv} in this paper.

During the spreading process, the contact line dissipation caused by the friction force at the contact line can be calculated through [49]:

$$W_{cl} = \frac{\pi D_m^2}{4}\sigma_{GL}(cos\,\theta_Y - cos\,\theta_{adv}) \tag{33}$$

Therefore, summing up Eqs. (30), (31) and (33), W can be expressed as:

$$W = \frac{\pi}{16}\frac{\rho u_0^2 D_m^3}{\sqrt{Re}} + \alpha\frac{\pi}{16}\frac{\rho u_c^2 D_m^3}{\sqrt{Re_c}} + \frac{\pi D_m^2}{4}\sigma_{GL}(cos\,\theta_Y - cos\,\theta_{adv}) \tag{34}$$

Then, substitute Eqs. (22), (26), (27) and (34) into Eq. (21), and introduce the maximum spread factor D_m^*, which is defined as $D_m^* = D_m/D_0$, ΔA_{GL} can be expressed as:

$$\Delta A_{GL} = \frac{\rho\frac{\pi D_0^3}{6}\left(0.5u_0^2 + g\left(H_0 - \frac{D_0}{3{D_m^*}^2}\right)\right) - \frac{\pi}{16}\frac{\rho u_0^2 D_0^3 {D_m^*}^3}{\sqrt{Re}} - \alpha\frac{\pi}{16}\frac{\rho u_c^2 D_0^3 {D_m^*}^3}{\sqrt{Re_c}}}{\sigma_{GL}} + \frac{\pi D_0^2 {D_m^*}^2}{4}\cos\theta_{adv} \tag{35}$$

The dimensionless maximum gas-liquid interfacial area is defined as $A_{GLm}^* = A_{GLm}/A_{GL0} = 1 + \Delta A_{GL}/A_{GL0}$, where $A_{GL0} = \pi {D_0}^2$, A_{GLm} is the maximum gas-liquid interfacial area. Therefore, A_{GLm}^* can be expressed as:

$$A_{GLm}^* = 1 + \frac{\frac{\rho D_0}{6}\left(0.5u_0^2 + g\left(H_0 - \frac{D_0}{3{D_m^*}^2}\right)\right) - \frac{\rho u_0^2 D_0 {D_m^*}^3}{16\sqrt{Re}} - \alpha\frac{\rho u_c^2 D_0 {D_m^*}^3}{16\sqrt{Re_c}}}{\sigma_{GL}} + \frac{{D_m^*}^2}{4}\cos\theta_{adv} \tag{36}$$

4.2. Results comparison

The maximum spread factor D_m^* is a critical factor for calculating the A_{GLm}^* by Eq. (36). In addition to the experimental measurements, a series of models for predicting D_m^* have been developed based on different approaches [14, 41-45, 48-53]. Several widely used or recently established models [43, 48, 53] were selected for predicting the D_m^* in Case 1-6, and the predicted results were compared with the results from the experimental measurements and CFD simulations, as shown in Fig. 13. Cases 7 and 8 were not used for comparison because of the asymmetry and fragmentation of the droplets. In Cases 1-4, the difference of the predicted D_m^* by the Ukiwe and Kwok model [43] and the experimental data is within 20% , but D_m^* is underestimated in Cases 5-6, where a high viscosity liquid was used. The Vadillo et al. model [53] gave a slightly better prediction of D_m^* than the Ukiwe and Kwok model for Cases 1-4, but

569 D_m^* was also underestimated in Cases 5-6. This means the above two models are not suitable for high
570 viscosity liquids. The Yonemoto and Kunugi model [48] overestimated D_m^* by about 25% in all the cases
571 except Case 4, where the D_m^* was massively underestimated. In the Yonemoto and Kunugi model [48],
572 the simple averaged contact angle of the static and advancing contact angles are used. Since the
573 static contact angles were not reported in the references for the experimental data, they were calculated
574 according to the Tadmor model [66], which might produce some deviations. The Huang and Chen
575 model [45] gave a better prediction of D_m^* compared with the other theoretical models except Case 4,
576 where a hydrophilic surface was used. For Case 4, the predicted D_m^* by the Huang and Chen model [45]
577 was about 16% higher than the experimental data, but it was close to the CFD simulation result. The
578 error is likely a result of the difficulty in accurately measuring the very small contact angle of the
579 employed hydrophilic surface. Therefore, the model developed by Huang and Chen [45] was
580 recommended for predicting D_m^* in this paper, and it is expressed as follows:

$$\begin{aligned}
&\frac{3}{4}\left(\frac{We}{\sqrt{Re}}+\frac{We_c}{\sqrt{Re_c}}\right){D_m^*}^4+3(1-cos\,\theta_{adv}){D_m^*}^3-(We+12)D_m^*+8=0, u_0<u_c,\\
&\frac{3}{4}\left(\frac{We_c}{\sqrt{Re_c}}\frac{Re_c}{Re}+\frac{We}{\sqrt{Re}}\right){D_m^*}^4+3(1-cos\,\theta_{adv}){D_m^*}^3-(We+12)D_m^*+8=0, u_0\geq u_c
\end{aligned} \tag{37}$$

581 where $We^*=\rho D_0 {u_c}^2/\sigma_{GL}$, $Re_c=\rho D_0 u_c/\mu$ and u_c is expressed in Eq. (32).

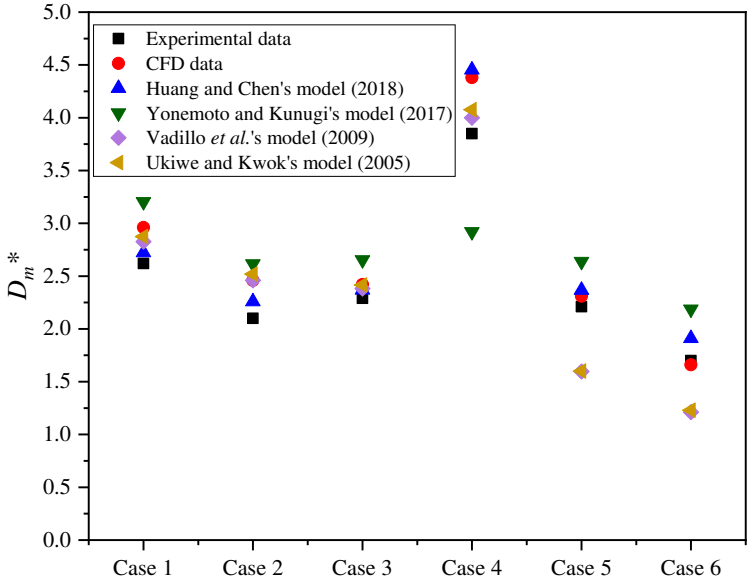

582

583 **Fig. 13**. Comparison of the D_m^* predicted by different theoretical models [43, 45, 48, 53] with the
584 experimental and CFD simulation results for the investigated cases [14-16, 23, 24].

585 At present, the widely used maximum gas-liquid interfacial area model is the cylindrical model

[43], which assumes that the droplet spreads into a cylindrical disk with a base diameter D_m at the maximum spread. The gas-liquid interfacial area is the sum of the top surface area and the side area of the cylinder, and A^*_{GLm} is expressed as follows:

$$A^*_{GLm} = \frac{A_{GLm}}{A_{GL0}} = \frac{\frac{\pi {D_m}^2}{4} + \pi D_m \frac{2D_0^3}{3D_m^2}}{\pi {D_0}^2} = \frac{{D_m^*}^2}{4} + \frac{2}{3D_m^*} \tag{38}$$

In addition, similar to Eq. (36), different A^*_{GLm} models can be derived by using different combinations of dissipation works and contact angles. Two models were developed by us based on the equations in literatures [43, 53], and the predicted results by these models are shown in Fig. 14. The D^*_m used in these models were calculated by Eq. (37). Since there was no available experimental data of the gas-liquid interfacial area, the CFD simulation results were used as a reference for comparisons. Since most of the models were not applicable to high viscosity droplets, only Cases 1 – 4 were used for comparing the prediction results. The predicted results from all these models show a consistent variation trend. In addition, the difference between the A^*_{GLm} predicted by Eq. (36) and from CFD simulations is within 12%. The maximum differences between the prediction results based on the models of Vadillo et al. [53] and Ukiwe et al. [43] and the simulation results are 20% and 25%, respectively. For the cylindrical model Eq. (38), the differences between the predicted A^*_{GLm} and the CFD simulation results are within 16%.

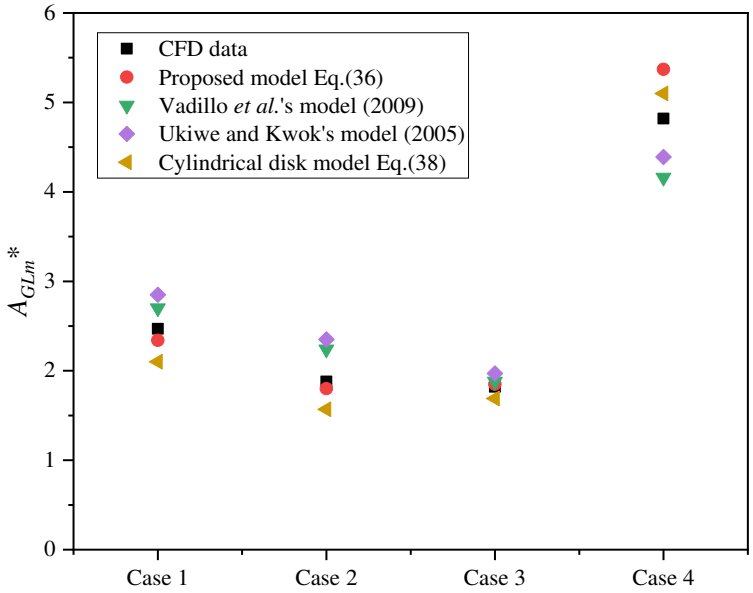

Fig. 14. Comparison of the $A_{GLm}{}^*$ from the CFD simulation and different models.

4.3. Remarks on the maximum gas-liquid interfacial area model

In this paper, a maximum gas-liquid interfacial area correlation is derived from analysing the energy conversion of the droplet when it impacts on a solid surface, which has shown a good prediction performance. Compared with the shape approximation methods, the energetic modelling method can clearly identify the main factors that affect the change of the gas-liquid interfacial area. It can be seen from the model that increasing the impact velocity, reducing the surface tension of the liquid, and reducing the gas-liquid advancing contact angle can promote the increase of the gas-liquid interfacial area. The higher the viscosity of the liquid, the more energy is dissipated during the impact, which weakens the increase in the gas-liquid interfacial area. In engineering applications, identifying major and minor factors that affect the change of the interfacial area can provide guidance for optimization. The accuracy of the model depends largely on the calculation of the dissipative work. Therefore, further efforts should be made to better describe the effect of dissipation. Also, accurately describing the evolution of the dynamic contact angle during the droplet impact on the solid surface is a way to improve the accuracy of the model, which is currently still a topic of ongoing research. In addition, D_m^* is a critical parameter for influencing the accuracy of all the interfacial area predictive models. Therefore, developing high reliability D_m^* models with a broad adaptive condition is very important for predicting the gas-liquid interfacial area accurately.

5. Conclusions

(i) Both 2D and 3D CFD simulations have been performed to investigate the variation of the interfacial areas when droplets impact on solid surfaces. In order to obtain the accurate data of interfacial areas, the VOF model with the dynamic contact angle and the local grid refinement techniques have been used, and the dynamic behaviours of the droplets have been accurately reproduced. The CFD model was validated through comparing with the available experimental data from experiments conducted over a wide range of surface properties and liquid properties.

(ii) The simulation results show that the gas-liquid interfacial area slightly decreases at the kinetic stage, then increases at the spreading stage, and it reaches the maximum at the end of the spreading stage. A large initial impact velocity leads to a large increase in the gas-liquid interfacial area, while a

high viscosity weakens the increase in the interface area due to the increase in dissipation work. For the droplet impact on a hydrophilic surface, the hydrophilic surface can promote the increase in the gas-liquid interfacial area by releasing the liquid-solid interface energy. Meanwhile, for the droplet impacting on a hydrophobic surface, the gas-liquid interfacial area can be enhanced by breaking up the droplet into small droplets.

(iii) By analysing the energy conversion of the droplet impact on a solid surface, a new correlation for predicting the maximum gas-liquid interfacial area of the droplet has been proposed. The accurate dissipative work equation is the basis of the accurate prediction of the gas-liquid interface area. Compared with the CFD simulation results and other models, the new correlation has been shown to be a good prediction of the performance. In addition, this study leads to a much better understanding of the behaviour of the interface areas when droplets impact on a solid surface.

Acknowledgement

The authors acknowledge the financial support from the EPSRC under grant EP/M001458/2, the National Natural Science Foundation of China under Grant 51876143, the State Grid Corporation of China under Grant SGRIWLZXQT[2017]882. In addition, P. Xie and H. Ding would like to acknowledge the China Scholarship Council and the University of Sheffield for funding their research studies.

Nomenclature

A_{GL}	gas-liquid interfacial area
A_{SG}	solid-gas interfacial area
A_{SL}	solid-liquid interfacial area
A_0	initial gas-liquid interfacial area of the droplet
A^*	gas-liquid interfacial area factor
D	the diameter of the liquid-solid contact interface
D_0	initial droplet diameter
D_m	maximum spread diameter
D_m^*	maximum spread factor

E_k	the initial kinetic energy
E_P	the potential energy
E_s	the total surface energy
f_{vol}	surface tension source term
h_m	hight of the droplet at the maximum spread
k	the curvature of the interface
N	unit normal vector
p	pressure
t^*	dimensionless time
t_c	the characteristic time
t_m	time at the end of the spreading stage
t_m^*	maximum spreading dimensionless time
u	velocity
u_{cl}	contact line velocity
u_0	initial impact velocity
W	the energy loss due to dissipation

Greek symbols

A	volume fraction
θ_{adv}	advancing contact angle
θ_d	dynamic contact angle
θ_{rec}	receding contact angle
ε_L	liquid holdup
μ	dynamic viscosity
ν	kinematic viscosity
ρ	density
σ_{GL}	surface tension coefficient of liquid
σ_{SG}	the solid-gas interfacial energy
σ_{SL}	the solid-liquid interfacial energy
φ	signed distance to the interface in level-set method
Φ	viscous dissipation function
Ω	the volume where the dissipation occurs
δ	thickness of the boundary layer

Subscripts

G	gas phase
L	liquid phase

Abbreviations

Ca	capillary number
Oh	Ohnesorge number
Re	Reynolds number
We	Weber number
WFM	wetting force model

References

[1] Y. Cheng, F. Wang, J. Xu, D. Liu, Y. Sui, Numerical investigation of droplet spreading and heat transfer on hot substrates, Int. J. Heat Mass Transfer, 121 (2018) 402-411.

[2] Deendarlianto, Y. Takata, A. Widyatama, A.I. Majid, A. Wiranata, A. Widyaparaga, M. Kohno, S. Hidaka, Indarto, The interfacial dynamics of the micrometric droplet diameters during the impacting onto inclined hot surfaces, Int. J. Heat Mass Transfer, 126 (2018) 39-51.

[3] Z. Wang, Y.M. Xing, X. Liu, L. Zhao, Y.B. Ji, Computer modeling of droplets impact on heat transfer during spray cooling under vibration environment, Appl. Therm. Eng., 107 (2016) 453-462.

[4] X.M. Wu, Z. Qin, Y.S. Yu, Z.X. Zhang, Experimental and numerical study on CO2 absorption mass transfer enhancement for a diameter-varying spray tower, Appl. Energy, 225 (2018) 367-379.

[5] J. Baldyga, J.R. Bourne, B. Zimmermann, Investigation of Mixing in Jet Reactors Using Fast, Competitive Consecutive Reactions, Chem. Eng. Sci., 49(12) (1994) 1937-1946.

[6] S. Sen, V. Vaikuntanathan, D. Sivakumar, Experimental investigation of biofuel drop impact on stainless steel surface, Exp Therm Fluid Sci, 54 (2014) 38-46.

[7] E. Kompinsky, G. Dolan, E. Sher, Experimental study on the dynamics of binary fuel droplet impacts on a heated surface, Chem. Eng. Sci., 98 (2013) 186-194.

[8] H.-J. Chang, M.H. Tsai, W.-S. Hwang, The simulation of micro droplet behavior of molten lead-free solder in inkjet printing process and its experimental validation, Appl Math Model, 36(7) (2012) 3067-3079.

[9] S. Fathi, P. Dickens, F. Fouchal, Regimes of droplet train impact on a moving surface in an additive manufacturing process, J Mater Process Tech, 210(3) (2010) 550-559.

[10] D. Khojasteh, M. Kazerooni, S. Salarian, R. Kamali, Droplet impact on superhydrophobic surfaces: A review of recent developments, J Ind Eng Chem, 42 (2016) 1-14.

[11] C. Josserand, S.T. Thoroddsen, Drop Impact on a Solid Surface, Annu Rev Fluid Mech, 48 (2016) 365-391.

[12] A.L.N. Moreira, A.S. Moita, M.R. Panão, Advances and challenges in explaining fuel spray impingement: How much of single droplet impact research is useful?, Prog Energ Combust, 36(5) (2010) 554-580.

[13] A.L. Yarin, Drop impact dynamics: Splashing, spreading, receding, bouncing... Annual Review of Fluid Mechanics, 38 (2006) 159-192.

[14] T. Mao, D.C.S. Kuhn, H. Tran, Spread and rebound of liquid droplets upon impact on flat surfaces, AlChE J., 43(9) (1997) 2169-2179.

[15] R. Rioboo, M. Marengo, C. Tropea, Time evolution of liquid drop impact onto solid, dry surfaces, Exp Fluids, 33(1) (2002) 112-124.

[16] S. Sikalo, M. Marengo, C. Tropea, E.N. Ganic, Analysis of impact of droplets on horizontal surfaces, Exp Therm Fluid Sci, 25(7) (2002) 503-510.

[17] M. Tembely, R. Attarzadeh, A. Dolatabadi, On the numerical modeling of supercooled micro-droplet impact and freezing on superhydrophobic surfaces, Int. J. Heat Mass Transfer, 127 (2018) 193-202.

[18] X. Wang, D.-L. Sun, X.-D. Wang, W.-M. Yan, Dynamics of droplets impacting hydrophilic surfaces decorated with a hydrophobic strip, Int. J. Heat Mass Transfer, 135 (2019) 235-246.
[19] L. Wang, S. Rong, S. Shen, T. Wang, Z. Che, Interface oscillation of droplets upon impact on a heated surface in the Leidenfrost state, Int. J. Heat Mass Transfer, 148 (2020) 119116.
[20] Z.B. Wang, R. Chen, X. Zhu, Q. Liao, D.D. Ye, B. Zhang, X.F. He, L. Jiao, Dynamic behaviors of the coalescence between two droplets with different temperatures simulated by the VOF method, Appl. Therm. Eng., 131 (2018) 132-140.
[21] Z. Zhang, H.F. Liu, F. Zhang, M.F. Yao, Numerical study of spray micro-droplet impinging on dry/wet wall, Appl. Therm. Eng., 95 (2016) 1-9.
[22] M. Bussmann, S. Chandra, J. Mostaghimi, Modeling the splash of a droplet impacting a solid surface, Phys Fluids, 12(12) (2000) 3121-3132.
[23] Š. Šikalo, H.-D. Wilhelm, I. Roisman, S. Jakirlić, C. Tropea, Dynamic contact angle of spreading droplets: Experiments and simulations, Phys Fluids, 17(6) (2005) 062103.
[24] K. Yokoi, D. Vadillo, J. Hinch, I. Hutchings, Numerical studies of the influence of the dynamic contact angle on a droplet impacting on a dry surface, Phys Fluids, 21(7) (2009).
[25] P. Xie, X.S. Lu, H.B. Ding, X. Yang, D. Ingham, L. Ma, M. Pourkashanian, A mesoscale 3D CFD analysis of the liquid flow in a rotating packed bed, Chem. Eng. Sci., 199 (2019) 528-545.
[26] P. Xie, X. Lu, X. Yang, D. Ingham, L. Ma, M. Pourkashanian, Characteristics of liquid flow in a rotating packed bed for CO_2 capture: A CFD analysis, Chem. Eng. Sci., 172 (2017) 216-229.
[27] Y. Sui, H. Ding, P.D.M. Spelt, Numerical Simulations of Flows with Moving Contact Lines, Annual Review of Fluid Mechanics, Vol 46, 46 (2014) 97-119.
[28] T. Omori, T. Kajishima, Apparent and microscopic dynamic contact angles in confined flows, Phys Fluids, 29(11) (2017).
[29] H. Ding, P. Xie, D. Ingham, L. Ma, M. Pourkashanian, Flow behaviour of drop and jet modes of a laminar falling film on horizontal tubes, Int. J. Heat Mass Transfer, 124 (2018) 929-942.
[30] M. Pasandideh-Fard, S.D. Aziz, S. Chandra, J. Mostaghimi, Cooling effectiveness of a water drop impinging on a hot surface, Int J Heat Fluid Fl, 22(2) (2001) 201-210.
[31] J.E. Seebergh, J.C. Berg, Dynamic wetting in the low capillary number regime, Chem. Eng. Sci., 47(17) (1992) 4455-4464.
[32] S.F. Kistler, Hydrodynamics of wetting, Wettability, 6 (1993) 311-430.
[33] T.-S. Jiang, O.H. Soo-Gun, J.C. Slattery, Correlation for dynamic contact angle, J. Colloid Interface Sci., 69(1) (1979) 74-77.
[34] Y.D. Shikhmurzaev, Capillary flows with forming interfaces, Chapman and Hall/CRC, 2007.
[35] I. Malgarinos, N. Nikolopoulos, M. Marengo, C. Antonini, M. Gavaises, VOF simulations of the contact angle dynamics during the drop spreading: standard models and a new wetting force model, Adv. Colloid Interface Sci., 212 (2014) 1-20.
[36] C. Antonini, F.J. Carmona, E. Pierce, M. Marengo, A. Amirfazli, General Methodology for Evaluating the Adhesion Force of Drops and Bubbles on Solid Surfaces, Langmuir, 25(11) (2009) 6143-6154.
[37] A. Theodorakakos, G. Bergeles, Simulation of sharp gas–liquid interface using VOF method and adaptive grid local refinement around the interface, Int. J. Numer. Methods Fluids, 45(4) (2004) 421-439.
[38] I. Malgarinos, N. Nikolopoulos, M. Gavaises, Coupling a local adaptive grid refinement technique with an interface sharpening scheme for the simulation of two-phase flow and free-surface flows using VOF methodology, J. Comput. Phys., 300 (2015) 732-753.
[39] Z. Jian, C. Josserand, S. Popinet, P. Ray, S. Zaleski, Two mechanisms of droplet splashing on a solid substrate, J Fluid Mech, 835 (2017) 1065-1086.
[40] R. Cimpeanu, D.T. Papageorgiou, Three-dimensional high speed drop impact onto solid surfaces at arbitrary angles, Int J Multiphas Flow, 107 (2018) 192-207.
[41] S. Chandra, C. Avedisian, On the collision of a droplet with a solid surface, Proceedings of the Royal Society of London. Series A: Mathematical and Physical Sciences, 432(1884) (1991) 13-41.
[42] M. PasandidehFard, Y.M. Qiao, S. Chandra, J. Mostaghimi, Capillary effects during droplet impact on a solid surface, Phys Fluids, 8(3) (1996) 650-659.

[43] C. Ukiwe, D.Y. Kwok, On the maximum spreading diameter of impacting droplets on well-prepared solid surfaces, Langmuir, 21(2) (2005) 666-673.
[44] J.B. Lee, D. Derome, R. Guyer, J. Carmeliet, Modeling the Maximum Spreading of Liquid Droplets Impacting Wetting and Nonwetting Surfaces, Langmuir, 32(5) (2016) 1299-1308.
[45] H.-M. Huang, X.-P. Chen, Energetic analysis of drop's maximum spreading on solid surface with low impact speed, Phys Fluids, 30(2) (2018) 022106.
[46] H. Park, W.W. Carr, J. Zhu, J.F. Morris, Single drop impaction on a solid surface, AlChE J., 49(10) (2003) 2461-2471.
[47] X. Gao, R. Li, Spread and recoiling of liquid droplets impacting solid surfaces, AlChE J., 60(7) (2014) 2683-2691.
[48] Y. Yonemoto, T. Kunugi, Analytical consideration of liquid droplet impingement on solid surfaces, Scientific reports, 7(1) (2017) 1-11.
[49] F. Wang, L. Yang, L. Wang, Y. Zhu, T. Fang, Maximum Spread of Droplet Impacting onto Solid Surfaces with Different Wettabilities: Adopting a Rim–Lamella Shape, Langmuir, 35(8) (2019) 3204-3214.
[50] I.V. Roisman, R. Rioboo, C. Tropea, Normal impact of a liquid drop on a dry surface: model for spreading and receding, Proceedings of the Royal Society of London. Series A: Mathematical, Physical and Engineering Sciences, 458(2022) (2002) 1411-1430.
[51] X. Liu, X. Zhang, J. Min, Spreading of droplets impacting different wettable surfaces at a Weber number close to zero, Chem. Eng. Sci., 207 (2019) 495-503.
[52] N. Laan, K.G. de Bruin, D. Bartolo, C. Josserand, D. Bonn, Maximum Diameter of Impacting Liquid Droplets, Physical Review Applied, 2(4) (2014) 044018.
[53] D. Vadillo, A. Soucemarianadin, C. Delattre, D. Roux, Dynamic contact angle effects onto the maximum drop impact spreading on solid surfaces, Phys Fluids, 21(12) (2009) 122002.
[54] C.W. Hirt, B.D. Nichols, Volume of fluid (VOF) method for the dynamics of free boundaries, J. Comput. Phys., 39(1) (1981) 201-225.
[55] J.U. Brackbill, D.B. Kothe, C. Zemach, A continuum method for modeling surface tension, J. Comput. Phys., 100(2) (1992) 335-354.
[56] F. Gibou, R. Fedkiw, S. Osher, A review of level-set methods and some recent applications, J. Comput. Phys., 353 (2018) 82-109.
[57] M. Raw, Robustness of coupled algebraic multigrid for the Navier-Stokes equations, in: 34th Aerospace sciences meeting and exhibit, 1996, pp. 297.
[58] A. Al-Sharafi, B.S. Yilbas, H. Ali, Water droplet mobility on a hydrophobic surface under a thermal radiative heating, Appl. Therm. Eng., 128 (2018) 92-106.
[59] X.S. Wu, Y. Luo, G.W. Chu, Y.C. Xu, L. Sang, B.C. Sun, J.F. Chen, Visual Study of Liquid Flow in a Spinning Disk Reactor with a Hydrophobic Surface, Ind. Eng. Chem. Res., 57(22) (2018) 7692-7699.
[60] J.P. Zhang, W. Liu, Y. Luo, G.W. Chu, H.K. Zou, J.F. Chen, Enhancing liquid droplet breakup by hydrophobic wire mesh: Visual study and application in a rotating packed bed, Chem. Eng. Sci., 209 (2019) 115180.
[61] I.V. Roisman, L. Opfer, C. Tropea, M. Raessi, J. Mostaghimi, S. Chandra, Drop impact onto a dry surface: Role of the dynamic contact angle, Colloid Surface A, 322(1-3) (2008) 183-191.
[62] A. Al-Sharafi, B.S. Yilbas, H. Ali, N. AlAqeeli, A water droplet pinning and heat transfer characteristics on an inclined hydrophobic surface, Scientific reports, 8(1) (2018) 1-20.
[63] D. Caviezel, C. Narayanan, D. Lakehal, Adherence and bouncing of liquid droplets impacting on dry surfaces, Microfluid Nanofluid, 5(4) (2008) 469-478.
[64] T. Young, III. An essay on the cohesion of fluids, Philosophical transactions of the royal society of London, (95) (1805) 65-87.
[65] T.S. Chow, Wetting of rough surfaces, J Phys-Condens Mat, 10(27) (1998) L445-L451.
[66] R. Tadmor, Line Energy and the Relation between Advancing, Receding, and Young Contact Angles, Langmuir, 20(18) (2004) 7659-7664.